D2.2 (AVHRR): Report on the AVHRR FCDR uncertainty

Michael Taylor (1), Jonathan Mittaz (1,2), Marine Desmons (1), Emma Woolliams (2)

(1) University of Reading, (2) National Physical Laboratory

7th August 2019

v1.1a

Contents

1 Introduction

1.1 Scope

This document is one of the five documents that make up the D2-2 report on traceability chains for FCDRs. Since the original project proposal our thoughts have refined and while this document describes the "sequence of measurement standards and calibrations that is used to relate a measurement result to a reference" (the VIM definition of a traceability chain), it is not presenting this in the form of a chain.

This document provides an overview of the uncertainty analysis for the sensors analysed along with the methods to establish metrological traceability for the developed FCDRs and is specifically about the AVHRR FCDR. Document D2-2a provides an overview of the purposes of these documents and explains the basis of the effects tables.

1.2 Version Control

Version	Reason	Reviewer	Date of Issue
1.0	Original submission deadline	Chris Merchant, Rhona Phipps	September 2017
1.1a	Draft for comment prior to end of project		August 2019
1.c			

1.3 Applicable and Reference Documents

1.3.1 D2-2 set of documents

D2-2a   : Principles behind the FCDR effects table
D2-2 (microwave): Report on the MW FCDR: Uncertainty
D2-2 (HIRS)   : Report on the HIRS FCDR: Uncertainty
D2-2 (AVHRR)   : Report on the AVHRR FCDR: Uncertainty (this document)
D2-2 (MVIRI)   : Report on the MVIRI FCDR: Uncertainty

1.3.2 References

Bicknell, W.E. (2000). HgCdTe Detector Responsivity and GOES Instrument Calibration, *GOES Project Report NOAA-3(R-1).*

Doelling, D. R., Bhatt, R., Scarino, B. R., Gopalan, A., Haney, C. O., Minnis, P., & Bedka, K. M. (2016). A Consistent AVHRR Visible Calibration Record Based on Multiple Methods Applicable for the NOAA Degrading Orbits. Part II: Validation. *Journal of Atmospheric and Oceanic Technology*, *33*(11), 2517-2534.

Heidinger, A.K., Straka W,C,, Molling, C.C., Sullivan, J.T. & Wu,X (2010) Deriving an inter-sensor consistent calibration for the AVHRR solar reflectance data record, International Journal of Remote Sensing, 31, 6493-6517 DOI: http://dx.doi.org/10.1080/01431161.2010.496472.

International Vocabulary of Metrology, VIM (2008). Evaluation of measurement data—guide for the expression of uncertainty in measurement. *JCGM* 100: 2008 (GUM 1995 with minor corrections).

Merchant, C, Mittaz, J., Woolliams, E. R., Scanlon, T., Dilo, A. (2015). D2-1: Metrological framework for the development of fundamental climate data records, FIDUCEO Report http://fiduceo.pbworks.com/w/file/97334616/D2_1 FCDR Framework for FCDR Development V1.0.pdf.

Merchant, C. J., Paul, F., Popp, T., Ablain, M., Bontemps, S., Defourny, P., Hollmann, R., Lavergne, T., Laeng, A., de Leeuw, G., Mittaz, J., Poulsen, C., Povey, A. C., Reuter, M., Sathyendranath, S., Sandven, S., Sofieva, V. F., and Wagner, W. (2017). Uncertainty information in climate data records from Earth observation, *Earth System Science Data*, 9, 511-527, https://doi.org/10.5194/essd-9-511-2017.

Mittaz, J. P., Harris, A. R., & Sullivan, J. T. (2009). A physical method for the calibration of the AVHRR/3 thermal IR channels 1: the prelaunch calibration data. *Journal of Atmospheric and Oceanic Technology,* 26(5), 996-1019.

Mittaz, J., & Harris, A. (2011). A physical method for the calibration of the AVHRR/3 thermal IR channels. Part II: An in-orbit comparison of the AVHRR longwave thermal IR channels on board MetOp-A with IASI. *Journal of Atmospheric and Oceanic Technology*, 28(9), 1072-1087.

Mittaz, J. (2011b), The Calibration of the Broadband Infrared Sensors Onboard NOAA Satellites, Proceedings of the GHRSST XII science team meeting, John McIntyre Conference Centre, Edinburgh 27th June - 1st July 2011, 270-276 (https://www.ghrsst.org/meetings/12th-international-ghrsst-science-team-meeting-ghrsst-xii/)

Mittaz, Bali & Harris (2013) The calibration of broad band infrared sensors: Time variable biases and other issues, EUMETSAT Meteorological satellite Conference, Vienna, 16-20 September 2013, https://www.eumetsat.int/website/wcm/idc/idcplg?IdcService=GET_FILE&dDocName=PDF_CONF_P_S8_11_MITTAZ_V&RevisionSelectionMethod=LatestReleased&Rendition=Web

Mittaz (2016) Instrument Noise characterization and the Allan/M-sample variance, FIDUCEO Report http://www.fiduceo.eu/content/instrument-noise-characterization-and-allanm-sample-variance

Mittaz, J., Merchant, C. J., & Woolliams, E. R. (2019). Applying principles of metrology to historical Earth observations from satellites. Metrologia, 56(3), 032002.

NASA-GSFC (1996). Performance Specification for the NOAA-K, L, M, N, N' & MetOp Advanced Very High Resolution Radiometer/3, S-480-81, Goddard Space Flight Center, NASA, Greenbelt, Maryland.

Podestá, G. P., Arbelo, M., Evans, R., Kilpatrick, K., Halliwell, V., & Brown, J. (2003). Errors in high- latitude SSTs and other geophysical products linked to NOAA- 14 AVHRR channel 4 problems. *Geophysical research letters*, *30*(11).

Theocharous, E., Theocharous, O. (2006). Practical limit of the accuracy of radiometric measurements using HgCdTe detectors, Applied Optics, 45, 7753-7759.

Trishchenko, A. P., & Li, Z.: (2001). A method for the correction of AVHRR onboard IR calibration in the event of short-term radiative contamination. International Journal of Remote Sensing, 22(17), 3619-3624.

Trishchenko, A. P. (2002). Removing unwanted fluctuations in the AVHRR thermal calibration data using robust techniques. *Journal of Atmospheric and Oceanic Technology*, 19(12), 1939-1954.

Trishchenko, A. P., G. Fedosejevs, L. Zhanqing, and J. Cihlar, 2002: Trends and uncertainties in thermal calibration of AVHRR radiometers onboard NOAA-9 to NOAA-16. *Journal of Geophysical Research*, 107, 4778, doi:10.1029/2002JD002353.

Walton, C. C., J. T. Sullivan, C. R. N. Rao, and M. Weinreb, 1998: Corrections for detector nonlinearities and calibration in- consistencies of the infrared channels of the Advanced Very High Resolution Radiometer. Journal of Geophysical Research, 103, 3323– 3337.

Wang, L. & Cao, C. (2008), On-Orbit Calibration Assessment of AVHRR Longwave Channels on MetOp-A Using IASI, IEEE Transactions on Geoscience and Remote Sensing, 46, 4005 – 4013, DOI: 10.1109/TGRS.2008.2001062.

Weinreb, M. P., Hamilton, G., Brown, S., & Koczor, R. J. (1990). Nonlinearity corrections in calibration of Advanced Very High Resolution Radiometer infrared channels. Journal of Geophysical Research: Oceans, 95(C5), 7381-7388.

Woolliams, E. R. (2014). Uncertainty analysis for filter radiometry based on the uncertainty associated with integrated quantities. International Journal of Thermophysics, 35(6-7), 1353-1365.

Woolliams, E. R., Mittaz, J. P., Merchant, C. J., Dilo, A., & Fox, N. P. (2016). Uncertainty and Correlation in Level 1 and Level 2 Products: A Metrologist's View. In: Living Planet Symposium, Vol. 740, p. 80.

Woolliams, E. R., Hueni, A., Gorroño, J. (2015). Intermediate Uncertainty Analysis for Earth Observation (Instrument Calibration), EMRP-ENV04-D5.2.2_textbook (version 2), http://www.meteoc.org/outreach-training.html.

Wu, X., J. J. Sullivan, J. J., and A. K. Heidinger, A. K. (2010). Operational calibration of the Advanced Very High Resolution Radiometer (AVHRR) visible and near-infrared channels, Canadian Journal of Remote Sensing 36, 602-616.

1.4 Glossary

AVHRR	Advanced Very High Resolution Radiometer
DSV	Deep Space View
FCDR	Fundamental Climate Data Record
ICT	Internal Calibration Target
IR	Infrared

IWCT	Internal Warm Calibration Target
MetOp	Meteorological Operational satellite
NEdT	Noise Equivalent delta Temperature
NOAA	National Oceanic and Atmospheric Administration
PFM	Pre-Flight Model
PRT	Platinum Resistance Thermometer
SRF	Spectral Response Function
TIROS	Television Infra-Red Observation Satellite
VIM	International Vocabulary of Metrology

Other definitions:

"Type A" and "Type B" refer to definitions from the Guide to Uncertainty in Measurement.
Type A is based on statistical analysis; Type B is based on expert judgement.

2 General Overview

A separate document, D2-2a gives an overview of errors and uncertainty, including how these have been considered in previous projects. The document also outlines how random and systematic uncertainties are handled separately, and how to account for the relationship and correlation that exists between the two. In FIDUCEO we have defined an effects table which describes:

- the uncertainty associated with a given effect
- the sensitivity coefficient required to propagate uncertainties associated with that effect to uncertainties associated with the measurand (Earth radiance, reflectance or brightness temperature)
- the correlation structure over spatial, temporal and spectral scales for errors resulting from this effect.

The concepts behind the effects tables are described in D2-2a. In this document we provide a discussion of the effects tables and uncertainty propagation for a single instrument series; here the AVHRR FCDR.

3 The AVHRR instrument

The Advanced Very High Resolution Radiometer (AVHRR) is a broadband, four or five channel (depending on the model) across-track scanner, that senses in the visible, near-infrared, and thermal infrared portions of the electromagnetic spectrum (see Table 2).

Cross-track scanning is accomplished by a continuously rotating scan mirror (oriented at 45 degrees with respect to the axis of rotation to avoid the variation of polarization effects across the swath) that is directly driven by a motor. The AVHRR flies on-board the National Oceanic and Atmospheric Administration's (NOAA's) Polar Orbiting Environmental Satellites (POES), since 1978 with TIROS-N, which is the first version of the instrument. Each pass of the satellite provides a 2399 km wide swath. The satellite orbits the Earth approximately 14 times each day from 833 km above its surface. The AVHRR instrument detects reflected solar and radiated thermal energy from land, sea, clouds and the atmosphere to provide global imagery (Cracknell, 1997).

Since TIROS-N, there have been 3 instances of AVHRR/1, 6 instances of AVHRR/2 (one of which failed to reach orbit) and 7 instances of AVHRR/3 (see Table 1). Differences between subsequent versions of AVHRR include a more rigorous pre-launch characterization and the addition of a sun shield in the case of AVHRR/3.

Table 1 A summary of the temporal coverage of the different AVHRR instruments

Generation	Satellite Name	Equator Crossing	Start time	End time
AVHRR/1	TIROS-N	AM	1978-10-19	1980-01-30
AVHRR/1	NOAA-6/A	AM	1979-06-27	1986-11-16
AVHRR/2	NOAA-7/C	PM	1981-08-24	1986-06-07
AVHRR/1	NOAA-8/E	AM	1983-05-03	1985-10-31
AVHRR/2	NOAA-9/F	PM	1985-02-25	1994-05-11
AVHRR/1	NOAA-10/G	AM	1986-11-17	1991-09-17
AVHRR/2	NOAA-11/H	PM	1988-11-08	1994-09-13
AVHRR/2	NOAA-12/D	AM	1991-05-14	1994-12-15
AVHRR/2	NOAA-13		Launch failure	

AVHRR/2	NOAA-14/J	PM	1994-12-30	2007-05-23
AVHRR/3	NOAA-15/K	AM	1998-05-13	Operational
AVHRR/3	NOAA-16/L	PM	2000-09-21	2014-06-09
AVHRR/3	NOAA-17/M	AM	2002-06-24	2013-04-09
AVHRR/3	NOAA-18/N	PM	2005-08-30	Operational
AVHRR/3	NOAA-19/N'	PM	2009-06-02	Operational
AVHRR/3	MetOp-A	AM	2007-06-20	Operational
AVHRR/3	MetOp-B	AM	2013-04-24	Operational

Table 2 Wavelength range for the AVHRR channels

Channel	AVHRR/1	AVHRR/2	AVHRR/3	Detector
1	0.58-0.68 μm	0.58-0.68 μm	0.58-0.68 μm	Si
2	0.725-1.1 μm	0.725-1.1 μm	0.725-1.1 μm	Si
3a			1.58-1.64 μm	Si
3b	3.55-3.93 μm	3.55-3.93 μm	3.55-3.93 μm	InSb
4	10.50-11.50 μm	10.50-11.50 μm	10.50-11.50 μm	HgCdTe
5	Channel 4 repeated	11.5-12.5 μm	11.5-12.5 μm	HgCdTe

The FCDR of interest is for visible and infrared radiances, though this document concentrates mainly on the infrared channels as we are using an external calibration for the visible channels. The thermal channels are calibrated before launch as well as in-flight, using measurements of an internal warm calibration target (IWCT) and of a cold (deep space) target (S). This allows us to evaluate the instrument response as it changes with time. The calibration cycle is undertaken during every full scan, i.e. about 40000 times per orbit. On short time scales (sub-orbital), the calibration results are used to account for the changes in the instrument response associated with variations in the instrument operating temperatures, which vary by up to 3 K around an orbit. On longer time scales (lifetime of the instrument), the instrument response can change because of other factors, such as deterioration of the detectors/optics etc.

The AVHRR is a scanning radiometer that collects pixels as a sequence of scan lines at right angles to the direction of travel of the satellite over the ground. The in-flight calibration procedure of the AVHRR consists of ten measurements (as counts) per scan line when viewing the IWCT and ten measurements per scan line of counts for a space view. Four PRTs measure the temperature of the IWCT and allow an estimate of the spectral radiance from the IWCT to be made using Planck's Law and the estimated emissivity. From the spectral radiance, the channel-integrated spectral radiance from the IWCT is calculated by integrating the spectral radiance across the (assumed known) spectral response function (SRF) of a given channel.

The basic quantity recorded is "counts", a digital number value that relates to the voltage seen over the detector and corresponds to the total incident radiance including instrument self-emission. In operation, all the detectors are actively cooled to a temperature of 105 K to reduce detector noise and increase sensitivity. The electronics have been configured such that the counts reduce with increasing radiance. In order to maintain a dynamic range, the voltage from the space view (or cold target) observations are actively electronically clamped and are used as a reference voltage. This means that the detected signal is implicitly the total radiance observed by the detectors at the time of observation minus the radiance observed by the detectors when viewing space. The recorded counts are the result of a conversion of the analogue detected signal to a 10-bit binary form within the instrument. While

most IR instruments have used the space view to determine the noise in the Earth view, the presence of residual electronics effects when the electronic clamp is determined are a factor to consider.

While radiances are calibrated in units of mW m^{-2} sr^{-1} cm, measurements are usually converted to Brightness Temperatures (BTs) in units of kelvin. The brightness temperature calculation assumes a monochromatic measurement and a Planckian source. The channel-integrated radiance $L_{ch}(T_b)$ is the weighted average of the black body radiance $L_{BB}(\lambda, T_b)$ at temperature T_b and wavelength λ calculated from the Planck function, weighted by the spectral response function of each channel $\xi_{ch}(\lambda)$:

$$L_{ch}(T_b) = \frac{\int \xi_{ch}(\lambda) L_{BB}(\lambda, T_b) \, d\lambda}{\int \xi_{ch}(\lambda) \, d\lambda} \qquad \textit{Eq 3-1}$$

Using Eq 3-1, it is straightforward to construct a lookup table to calculate the radiance as a function of brightness temperature or its inverse $T_b(L_{ch})$. Another approach is to use "band correction factors" (Weinreb et al., 1990) to convert radiance to brightness temperatures. These use a monochromatic assumption and use a fitted central wavenumber and temperature correction coefficients (usually denoted by *a* and *b*) to closely match the behavior of Eq. 3-1. The full procedure is described in detail by Weinreb et al. (1990).

3.1   The AVHRR measurement function

The calibration algorithms of the AVHRR have had numerous incarnations over the lifetime of the sensor (1978 to present). Originally no account was made for the nonlinearity of the 11 and 12µm HgCdTe detectors, whereas subsequent calibration schemes used a range of lookup tables or correction terms to deal with it. The current operational calibration is based on Walton et al. (1998) and consists of a two-step process with a linear radiance first being calculated which is then corrected using a quadratic correction term. As has been pointed out by Mittaz et al. (2009), this formulation is intrinsically problematic. It is also clear that using parameters derived from pre-launch data within this formulation gives rise to significant biases (Wang & Cao 2008, Mittaz & Harris 2011).

An improved calibration equation, from Mittaz & Harris (2011), is:

$$L_E = a_0 + \frac{(\varepsilon + a_1)\tilde{L}_{IWCT} - a_2 - a_3(\bar{C}_S - \bar{C}_{IWCT})^2}{(\bar{C}_S - \bar{C}_{IWCT})}(\bar{C}_S - C_E) + a_3(\bar{C}_S - C_E)^2 + a_4 f(T_{inst}) + 0 \qquad \textit{Eq 3-2}$$

where, the terms are:

a_0, a_1, a_2, a_3, a_4	Calibration coefficients determined through harmonisation. Note that the a_2 term is usually set to zero (see Section 5)
ε	Pre-launch estimated emissivity of the IWCT
$\tilde{L}_{ICT}$	Band-integrated radiance of the IWCT
C_E	Count signal observing the Earth

$\overline{C}_{\mathrm{S}}$	Averaged count signal observing deep space (average of all space-view measurements for this scanline and for 25 scanlines either side)
$\overline{C}_{\mathrm{IWCT}}$	Averaged count signal observing the internal warm calibration target (average of all space-view measurements for this scanline and for 25 scanlines either side)
$f\left(T_{\mathrm{inst}}\right)$	A function for the instrumental temperature that applies to this particular AVHRR instrument and corrects for orbital drift effects. The instrumental temperature used here as a proxy for thermal effects on the satellite is the averaged IWCT temperature over one orbit.
$+0$	Represents the assumptions underpinning the form of the equation, and in particular the assumption that there is no non-quadratic nonlinearity.

The band-integrated IWCT radiance is given by

$$\tilde{L}_{\mathrm{ICT}} = \int L_{\mathrm{BB}}\left(\lambda, T_{\mathrm{IWCT}}\right)\xi\left(\lambda\right)\mathrm{d}\lambda \approx \sum_{i} L_{\mathrm{BB}}\left(\lambda_i, T_{\mathrm{IWCT}}\right)\xi\left(\lambda_i\right)\delta_{\lambda i} + 0 \qquad \textit{Eq 3-3}$$

where $\xi\left(\lambda\right)$ is the relative spectral response function, normalised to unit area, $L_{\mathrm{BB}}\left(\lambda, T_{\mathrm{IWCT}}\right)$ represents the Planck radiance for a blackbody at temperature T_{IWCT} and the integral over wavelength, λ, and is practically realised numerically from tabulated values of the spectral response function at wavelengths λ_i. The +0 term represents the extent to which this summation does not represent the true integral.

Operationally, the temperature of the IWCT is calculated from a simple mean of the four temperatures obtained from the four platinum resistance thermometers (PRTs) mounted on the IWCT. Note that this implicitly assumes a planar temperature distribution across the IWCT. If the temperature distribution is more complex (as it likely is) there will be an error introduced by using the simple mean. The PRTs themselves are recorded as a count which is converted to temperature using a calibration equation expressed as a fifth order polynomial. The calibration coefficients for the PRTs were determined pre-launch through comparison with a more accurate thermometer at different temperatures.

3.2   Uncertainty Tree Diagram

The measurement function tree diagram for the AVHRR is given in Figure 1. The tree is designed to show the sources of uncertainty from their origin through to the uncertainty in the measurand (Mittaz, Merchant and Woolliams, 2019). On the outside of the tree are the origins of the uncertainty which range from those with a physical origin such detector/electronic noise sources (which will be purely random effects) to error sources in the estimate of the internal calibration target (IWCT) radiance which are related to the limited design of the IWCT and which can contain both random (such as noise on the PRT measurements) and systematic (such as errors in PRT calibration) components. Other sources of error are due to the difficulty in our ability to model complex effects such as the corrections required due to solar contamination of the IWCT or the impact of thermal gradients on the imperfect IWCT itself. There are also uncertainties related to errors introduced by our imperfect knowledge of each channels spectral response function. Then there are errors related to effects we cannot directly measure such as the variation in the nonlinearity of the HgCdTe detector due to changes in the photon flux (e.g. Theocharous & Theocharous 2006) which are known to be present but would need the detector itself to be measured in a laboratory to obtain estimates of uncertainty which is impossible as the detector itself has been launched into space. Note that we try to include

all possible sources of uncertainty, however small, in line with the requirements of metrological traceability.
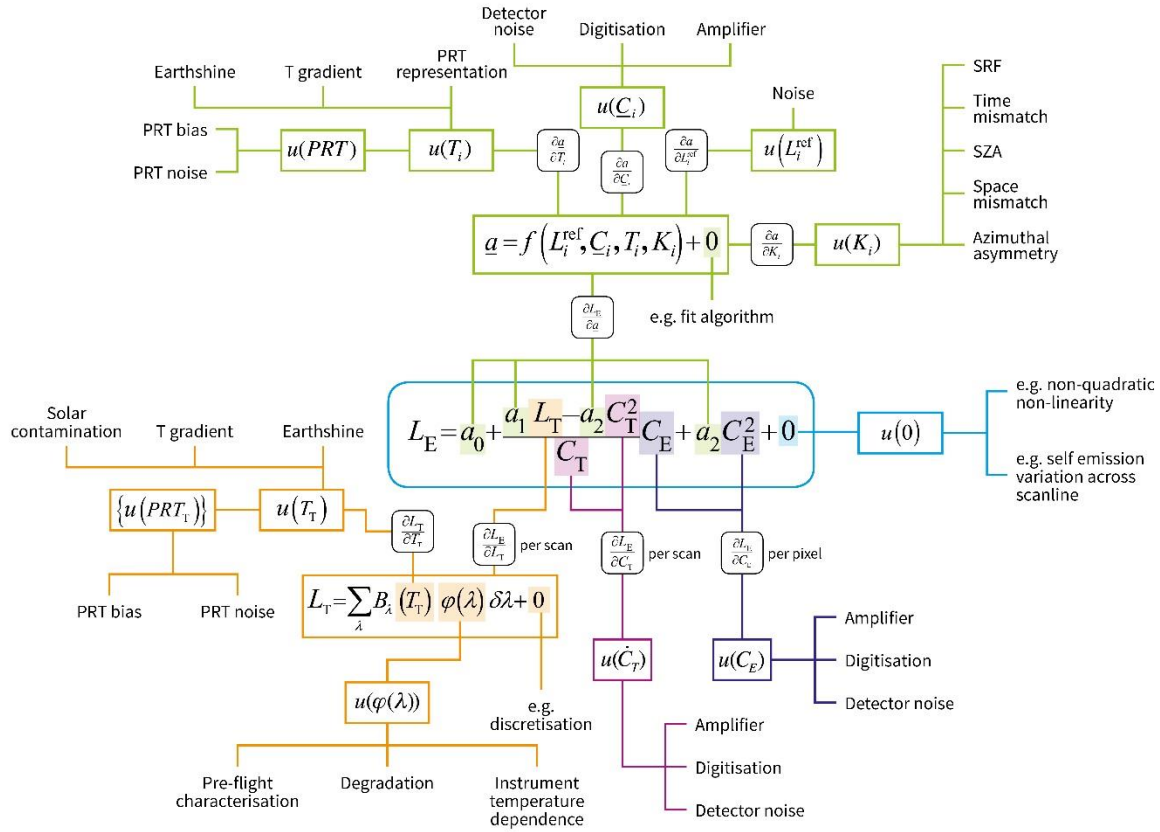

Figure 1 The measurement function tree for AVHRR. Note the measurement equation is a simplified form where $C_T = (\overline{C}_S - \overline{C}_{IWCT})$ *and* $C_E = (\overline{C}_S - C_{Earth})$. *Her also we have not included a temperature correction term related to changes in the satellites thermal environment as the orbit drits:* $a_3 f(T_{inst})$. *The nature of this term is still to be fully determined but is discussed further in the appendix.*

4   A discussion of different terms

In this section we consider the different sources of uncertainty and discuss the error correlation structure for this effect in the different dimensions using the Effects Tables that have been described in D2-2a. A full description of how these effects were evaluated is beyond the scope of this paper, but references are given, or details are provided in the appendices.

4.1   Noise in Earth Counts, Averaged Space Counts and Averaged IWCT Counts

Each detector has its own noise characteristics. There are a number of different noise sources that may be applicable for the AVHRR detectors including thermal noise (related to the detector temperature which as mentioned above for the AVHRR is held constant), shot noise (from statistical variations in the number of carriers which is itself a function of flux), 1/f noise from surface effects, noise generated by the electronics etc. We also have a range of detectors (Silicon for the visible/NIR channels, InSb for the 3.7µm channel and HdCdTe for the 11/12µm channels) which will each have their own noise characteristics.

It is actually quite difficult to measure the noise directly for the AVHRR. This is because observations of known sources (either space or the IWCT) only take 10 measurements at a time and, due to the variation of instrument temperature around an orbit, the observed total flux between measurements is not strictly constant. Further, the on-board digitisation itself can be of the order of the noise, which again makes an accurate measurement of the detector noise difficult. The Earth count noise is even harder to estimate because it is difficult to find Earth scenes that are sufficiently uniform to estimate any Earth count noise. Given that it is very difficult if not impossible to estimate the Earth count noise from the Earth view itself we have two possible noise sources to use. We can use either the noise estimated from the space view or use the noise estimated from the IWCT view. In the past people have tended to use the space view to determine the NeDT estimates because external radiance (space) is constant. In the case of the AVHRR, however, the space view is also when an electronic clamp is used to zero the counts to the radiance seen when looking at space adding a process which is unique to the space view data. Looking at the time variation of the noise derived from the space view (see Appendix) it also appears that the space view noise is more variable than the noise estimated derived from IWCT measurements so it is possible that the space clamp is adding signal to the measurements of the space view and so giving erroneous noise estimates. We have therefore taken the IWCT noise estimate as the Earth noise estimate rather than the more standard space view and the IWCT view data is taken under the same conditions as the Earth view unlike the space view. We also note that because we are using the Allan deviation to estimate the noise any variations in the IWCT view counts due to changing temperatures is automatically removed as the Allan deviation is not sensitive to such variations. A further discussion is given in Appendix A.1.

The Earth count is observed per pixel and therefore any noise associated with it will generally be independent from one pixel to another (it is a purely random effect). There may be a small exception to this rule for some AVHRR instruments where there has been observed cross-talk over time and between channels, see Appendix A.1 for more information.

The space and IWCT counts are, however, determined once per scanline and averaged as a simple rolling average across an averaging window of N scanlines (N/2 before and N/2 after) where N is sensor dependent and varies from 51 to 101. This means that all pixels on a scanline have a fully correlated error associated with IWCT and space observation noise and that the correlation from one scanline to another falls off as a triangle in the noise (see D2-2a). For most AVHRR instruments there is no correlation from spectral channel to spectral channel, though for the earliest AVHRR instrument on board TIROS-N there is some observed correlation between channels (see Appendix A.1). While the TIROS-N is not included in the time range specified for the AVHRR FCDR, it is discussed here

as it has provided physical understanding of, for example, electronics noise on other sensors that are included in the FCDR.

The effects tables for AVHRR counts are given in Table 3.

Table 3 Effects tables for the Earth, averaged-Space and averaged-IWCT counts

Table descriptor				
Name of effect		Earth Count Noise	Averaged Space Count Noise	Averaged IWCT Count Noise
Affected term in measurement function		C_E	$\bar{C}_S$	$\bar{C}_{IWCT}$
Instruments in the series affected		All	All	All
Correlation type and form	**Pixel-to-pixel [pixels]**	Random*	Rectangular Absolute	Rectangular Absolute
	from scanline to scanline [scanlines]	Random*	Triangular	Triangular
	between images [images]	N/A	N/A	N/A
	Between orbits [orbit]	Random	Random	Random
	Over time [time]	Random	Random	Random
Correlation scale	**Pixel-to-pixel [pixels]**	[0]	$[-\infty, +\infty]$	$[-\infty, +\infty]$
	from scanline to scanline [scanlines]	[0]	$n = 51$	$n = 51$
	between images [images]	N/A	N/A	N/A
	Between orbits [orbit]	[0]	[0]	[0]
	Over time [time]	[0]	[0]	[0]
Channels/ bands	**List of channels / bands affected**	All	All	All
	Correlation coefficient matrix	Identity matrix (1s down diagonal only)*	Identity matrix (1s down diagonal only)*	Identity matrix (1s down diagonal only)*
Uncertainty	**PDF shape**	Digitised Gaussian	Digitised Gaussian	Digitised Gaussian
	units	Counts	Counts	Counts

	magnitude	Provided per pixel	Provided per scanline?	Provided per scanline?
Sensitivity coefficient		$\dfrac{\partial L_E}{\partial C_E}$, Eq 4-1	$\dfrac{\partial L_E}{\partial \bar{C}_S}$, Eq 4-2	$\dfrac{\partial L_E}{\partial \bar{C}_{IWCT}}$, Eq 4-3

* For Tiros-N where there is cross-channel correlation and some pixel-to-pixel correlation in the noise, the correlation form is not random for the Earth counts and there are off-diagonal elements to the channel-to-channel correlation coefficient matrix.

The sensitivity coefficients are:

$$\frac{\partial L_E}{\partial C_E} = -\frac{\left(\varepsilon + a_1\right)\tilde{L}_{IWCT} - a_2 - a_3\left(\bar{C}_S - C_{IWCT}\right)^2}{\left(\bar{C}_S - \bar{C}_{IWCT}\right)} - 2a_3\left(\bar{C}_S - C_E\right) . \qquad \text{Eq 4-1}$$

$$\frac{\partial L_E}{\partial \bar{C}_S} = \frac{\left(\varepsilon + a_1\right)\tilde{L}_{IWCT} - a_2 - a_3\left(\bar{C}_S - \bar{C}_{IWCT}\right)^2}{\left(\bar{C}_S - \bar{C}_{IWCT}\right)} - $$
$$\frac{\left(\bar{C}_S - C_E\right)}{\left(\bar{C}_S - \bar{C}_{IWCT}\right)}\left[\frac{\left(\varepsilon + a_1\right)\tilde{L}_{IWCT} - a_2 - a_3\left(\bar{C}_S - \bar{C}_{IWCT}\right)^2}{\left(\bar{C}_S - \bar{C}_{IWCT}\right)} + 2a_3\left(\bar{C}_S - \bar{C}_{IWCT}\right)\right] + 2a_3\left(\bar{C}_S - C_E\right) \qquad \text{Eq 4-2}$$

$$\frac{\partial L_E}{\partial \bar{C}_{IWCT}} = \left(\bar{C}_S - C_E\right)\left[\frac{\left(\varepsilon + a_1\right)\tilde{L}_{IWCT} - a_2 - a_3\left(\bar{C}_S - \bar{C}_{IWCT}\right)^2}{\left(\bar{C}_S - \bar{C}_{IWCT}\right)^2} + a_3\right] \qquad \text{Eq 4-3}$$

4.2 Spectral response function

The spectral response functions of the different channels were determined pre-launch through an experimental characterisation and are defined by measurements at discrete wavelengths. The spectral response function is most significantly used in determining the band-integrated radiance of the IWCT and in determining the brightness temperature from the measured radiance.

The spectral response function is generally parametrized during pre-launch testing but the level of detail and accuracy can be variable over time. In the case of the AVHRR, the quality varies over time for a fairly meagre 20 measurements per SRF for the early AVHRRs, up to more than 200 listed values for the AVHRR/3 sensors. There is also always the possibility for a difference between measurements. One example is for NOAA-16 where the end-to-end measurements for the 12μm channel are different from the predicted values based on the responses of the individual optical components provided by the manufacturers. While the piece-part SRFs match reasonably well for the 3.7μm and 11μm channels, there is a clear discrepancy in the case of the 12μm channel (see Mittaz et al. 2009). Which is closer to the truth is, however, unknown at present. Apart from simple measurement errors there is also the possibility of changes in the SRF from pre-launch to in-orbit. This is especially apparent for channels that sit on an absorption lines. Within window channel regions such as are covered by the AVHRR IR channels the situation is not as clear cut as small variations in the SRF have only a small impact on the brightness temperatures as well as the fact that the fitted nonlinearity and a shift to the SRF are correlated (see Mittaz et al., 2009). This means that it is impossible to separate out an SRF shift from a change in the nonlinearity directly.

There are different types of uncertainty that are likely to have affected the original calibration of the spectral response function. In addition, the spectral response function is likely to have changed in orbit due to degradation of optical components, temperature sensitivities of the filters and any mismatch in optical illumination conditions (particularly angular) between calibration and use. These will have caused the following types of error:

- A systematic radiometric error in the SRF. Any error that applies equally (in a relative sense) to all wavelengths will effectively "cancel out" as the SRF used is the normalised SRF.
- A random radiometric error in the SRF. The effect of random noise in the SRF estimate that is random from one discrete wavelength value to the next, will be minimised through the spectral integration, if enough discrete values are combined in that integration.
- Any error that affects the width of the SRF and/or which is asymmetrical across the SRF (for example faster degradation at shorter wavelengths than longer wavelengths) will be significant
- Any systematic bias of the wavelength scale (a shift to shorter or longer wavelengths) will be significant.

In the current version of the Easy FCDR the SRF is the pre-launch SRF and no component of uncertainty has been assigned (see Appendix A.2). Due to the correlation between the nonlinearity and SRF, part of any SRF error will be removed during the non-linear coefficient harmonization but further work is needed - both on if an update to the SRF is needed, as well as to understand the implication for brightness temperature and whether an erroneous SRF will partially cancel out for some spectral bands where the scenes have a similar spectral shape to the IWCT.

The only SRF error term that will be considered in an effects table is a systematic wavelength shift which we currently have no estimate of. There is no correlation in the shift between channels, but the shift is considered identical for all measurements. It is therefore fully systematic, although the sensitivity coefficient will depend on local conditions.

Table 4 Effects tables for the SRF, considering a spectral shift

Table descriptor		
Name of effect		Spectral response function wavelength shift
Affected term in measurement function		$\xi(\lambda) \equiv \xi(\lambda + \delta_\lambda)$
Instruments in the series affected		All
Correlation type and form	**Pixel-to-pixel [pixels]**	Rectangular absolute
	from scanline to scanline [scanlines]	Rectangular absolute
	between images [images]	Rectangular absolute
	Between orbits [orbit]	Rectangular absolute
	Over time [time]	Rectangular absolute
	Pixel-to-pixel [pixels]	$\left[-\infty, +\infty\right]$

Correlation scale	from scanline to scanline [scanlines]	$[-\infty, +\infty]$
	between images [images]	$[-\infty, +\infty]$
	Between orbits [orbit]	$[-\infty, +\infty]$
	Over time [time]	$[-\infty, +\infty]$
Channels/bands	List of channels / bands affected	All
	Correlation coefficient matrix	Identity Matrix (no correlation)
Uncertainty	PDF shape	Gaussian
	Units	μm
	magnitude	Provided as a single value based on sensitivity analysis
Sensitivity coefficient		See Eq 4.7and Eq 4.8

4.3 IWCT Radiance effects

The IWCT radiance is calculated from Eq 3.3 assuming that the IWCT is a grey body with an emissivity $\varepsilon + a_3$ for a specific channel (we use value ε=0.985140 calculated from a theoretical estimate provided by the AVHRR manufacturer), and a temperature given by,

$$T_{\text{IWCT}} = \left(\frac{1}{N} \sum_i T_{\text{PRT},i} \right) + 0$$

Eq 4-4

As the simple mean of temperatures $T_{\text{PRT},i}$ measured by the $N = 4$ PRTs. The +0 here represents the assumption that the mean PRT signal is equal to the temperature of the IWCT averaged over the field of view of the radiometer. As well as the SRF wavelength shift, the band-integrated radiance of the IWCT is affected by the following components:

- Noise in individual PRT counts
- Systematic calibration bias of the PRTs
- Difference between radiant surface temperature at PRT location (front surface) and PRT measurement location (back of IWCT)
- Emissivity of IWCT
- Representativeness of the mean of the PRTs to the observed OWCT temperature
- Solar contamination of the IWCT

As these have different correlation structures they must be considered separately. Solar contamination and Earthshine are considered in the next section, Section 4.4).

The noise in the PRT counts is a structured random effect, it is random from one measurement to the next, but since the determined IWCT radiance is used for all pixels in a scanline and is averaged over several scanlines in a rolling average, the error in the IWCT radiance due to noise in the PRT measurements has a full correlation within a scanline and a triangular correlation from scanline to scanline. Because the noise in the individual PRTs are independent from one another, we can determine the uncertainty associated with noise in the mean PRT signal, which will be the noise in any individual PRT divided by $\sqrt{N}$. The noise associated with each individual PRT was investigated (Appendix A3.1). It is that noise that is included in the table above. Here the original noise is in counts but it is provided as a temperature error in kelvin.

The systematic calibration bias of the PRTs comes from the accuracy of the original PRT calibration, from any post-calibration drift and from the offset of the PRTs from the front surface of the IWCT. This is a fully systematic uncertainty component. The uncertainty is expressed in kelvin. Note that we do not consider uncertainties in the calibration coefficients for the fifth order polynomial used to convert counts to temperature. This is because those coefficients will be correlated and were determined from a temperature calibration and therefore it is better to think of uncertainties in terms of temperature. The uncertainty associated with the original calibration is treated as an effect of order 0.1 K, based on a conversation with PRT experts at NPL.

Since the PRTs are attached to the baseplate, which the IWCT sits on, the PRT is not measuring the temperature of the IWCT emitting surface itself but is measuring the base of the metal that makes up the IWCT. There is therefore the likelihood of an error between the radiant temperature at the location measured by the PRT and the PRT measured temperature. This error is very difficult to estimate given that no pre-launch measurements were made at the time of such an effect. An estimate of this has been made by Trishchenko et al. (2002) on the basis of the time variability of the measurements but without another study it is not clear if the effect looked at by Trishchenko et al. (2002) was related to a PRT/IWCT measurement issue or was related to problems with the operational calibration algorithm itself which has been shown to be physically wrong (e.g. Mittaz, Harris & Sullivan, 2009). It is also likely that the error in the IWCT temperature being the arithmetic mean maybe also be what Trishchenko and co-authors (2000, 2001, 2002) measured (see below).

Uncertainty in the emissivity of the IWCT is not considered. This is because the a_3 term, determined during harmonisation, is designed to correct any gross emissivity error. What has not been determined is if the IWCT emissivity changes over time due to degradation but the detection of such an effect is going to be very difficult if not impossible. So we are assuming in the harmonization process that the emissivity is time invariant.

The mean PRT measurement will not be representative of the observed temperature by the AVHRR instrument if there are non-linear thermal gradients across the IWCT. To estimate the possible extent of this, a study was performed (Appendix A.3.2) to understand the possible magnitude of error due to thermal gradients. This study showed that there were non-planar gradients across the IWCT and that these change over time; both short term (within an orbit) and over the longer term as the thermal environment becomes more extreme following orbital drifts (see also Appendix A.5 for further details). This effect will be correlated for relatively nearby scanlines (within an orbit and for similar orbital positions from one orbit to the next), but will be random over longer timescales and for points at different parts of the orbit. In Appendix A3.2 we analyse the scale of these correlations along scanlines and across orbits. In particular, we looked at the variation of the correlations at different temporal scales for both AVHRR/3 sensors onboard MetOp-A and NOAA-18, and also for the older AVHRR/1 sensor onboard NOAA-8 and the AVHRR/2 sensor onboard NOAA-7.

16

Four PRT temperatures are inadequate to determine much detail about the complex thermal gradients across the surface of the IWCT. We can, however, exploit understanding of the behaviour of the 3.7 μ m channel to constrain the problem. This channel uses an InSb detector which is known to be linear for the radiance levels observed from Earth observation. The 3.7 μ m channel gain is therefore expected to be constant around the orbit. We can then reasonably infer that significant deviations from a constant gain reflect errors in the ICT temperature estimate. A direct mapping from gain error to ICT temperature error constrained by the PRT measurements themselves can then be made (see Mittaz, Merchant and Woolliams, 2019). The corrected gain has lower variance, suggesting a substantial reduction in the ICT temperature error and the remaining variability in the 3.7 μ m channel gain can be used to estimate the ICT temperature uncertainty. The improved ICT temperature can then also be used to calibrate the 11 μ m and 12 μ m channels, where constant gain is not expected. This metrological approach estimates ICT temperature with reduced systematic errors, and provides a method to evaluate the remaining uncertainty, for propagation to uncertainty in measured radiances. This effect is also one that will introduce channel-to-channel error correlation because any remaining error in the ICT temperature will be present in the calibration of all the infrared channels (see Mittaz, Merchant and Woolliams, 2019).

Effects tables for these effects are given below. Note that because the IWCT temperature is calculated from the PRT signals and the IWCT band-integrated radiance is calculated for a specific channel from this temperature, all channels have a common error correlation due to these effects.

Table 5 Effects tables for the IWCT band-integrated radiance

Table descriptor				
Name of effect		PRT count noise	PRT bias and offset between baseplate and IWCT temperatures	PRT representativeness (thermal gradients)
Affected term in measurement function		$\tilde{L}_{\text{IWCT}}$	$\tilde{L}_{\text{IWCT}}$	$\tilde{L}_{\text{IWCT}}$
Instruments in the series affected		All	All	All
Correlation type and form	**Pixel-to-pixel [pixels]**	Rectangular Absolute	Rectangular Absolute	Rectangular Absolute
	from scanline to scanline [scanlines]	Triangular	Rectangular Absolute	Triangular Relative
	between images [images]	N/A	N/A	Unknown at the moment
	Between orbits [orbit]	Random	Rectangular Absolute	Unknown at the moment
	Over time [time]	Random	Rectangular Absolute	Random

Correlation scale	**Pixel-to-pixel [pixels]**	$\left[-\infty, +\infty\right]$	$\left[-\infty, +\infty\right]$	$\left[-\infty, +\infty\right]$
	from scanline to scanline [scanlines]	n = 51	$\left[-\infty, +\infty\right]$	$(-N, +N)$ where N is AVHRR sensor specific
	between images [images]	N/A	N/A	None
	Between orbits [orbit]	[0]	$\left[-\infty, +\infty\right]$	None
	Over time [time]	[0]	$\left[-\infty, +\infty\right]$	Unknown at the moment
Channels/ bands	**List of channels / bands affected**	All	All	All
	Correlation coefficient matrix	Matrix of 1s everywhere	Matrix of 1s everywhere	Matrix of 1s everywhere
Uncertainty	**PDF shape**	Gaussian	Gaussian	Guassian
	units	Counts (kelvin)	kelvin	kelvin
	magnitude	Provided per orbit? Or as a single value for all time? This should be uncertainty associated with the average PRT count due to noise individual counts.	0.1 K everywhere	Estimated from corrected 3.7 μ m channel gain variance
Sensitivity coefficient		$\dfrac{\partial L_{\mathrm{E}}}{\partial T_{\mathrm{IWCT}}}$, Eq.4-5	$\dfrac{\partial L_{\mathrm{E}}}{\partial T_{\mathrm{IWCT}}}$, Eq.4-5	$\dfrac{\partial L_{\mathrm{E}}}{\partial T_{\mathrm{IWCT}}}$, Eq.4-5

We can write, with a chain rule:

$$\frac{\partial L_{\mathrm{E}}}{\partial T_{\mathrm{IWCT}}} = \frac{\partial L_{\mathrm{E}}}{\partial \tilde{L}_{\mathrm{IWCT}}} \frac{\partial \tilde{L}_{\mathrm{IWCT}}}{\partial T_{\mathrm{IWCT}}} \qquad \textit{Eq 4-5}$$

where,

$$\frac{\partial L_{\mathrm{E}}}{\partial \tilde{L}_{\mathrm{IWCT}}} = \frac{\left(\varepsilon + a_1\right)}{\left(\bar{C}_{\mathrm{S}} - \bar{C}_{\mathrm{IWCT}}\right)} . \qquad \textit{Eq 4-6}$$

$$\frac{\partial \tilde{L}_{\mathrm{IWCT}}}{\partial T_{\mathrm{IWCT}}} = \sum_i \xi\left(\lambda_i\right) \delta_{\lambda i} \left.\frac{\partial L_{\mathrm{BB}}}{\partial T_{\mathrm{IWCT}}}\right|_{\left(\lambda_i, T_{\mathrm{IWCT}}\right)} \qquad \textit{Eq 4-7}$$

$$\left.\frac{\partial L_{\mathrm{BB}}}{\partial T_{\mathrm{IWCT}}}\right|_{(\lambda_i, T_{\mathrm{IWCT}})} = \frac{L_{\mathrm{BB}}(\lambda_i, T_{\mathrm{IWCT}})hc}{\lambda_i k_{\mathrm{B}} T_{\mathrm{IWCT}}^2 (1 - \exp[-hc/\lambda_i k_{\mathrm{B}} T_{\mathrm{IWCT}}])} \qquad \textit{Eq 4-8}$$

4.4 Solar contamination

4.4.1 Solar contamination

There are points in the orbit where the sun shines (directly or indirectly) onto the IWCT. This has 3 effects:

- In the 3.7µm channel sunlight is reflected off the IWCT into the calibration system (and was not corrected operationally until 1995).
- For all channels – sunlight heats the IWCT in a non-even way which may mean that the radiance calculated from the average of the four PRT readings is not representative of the measured radiance by the detector.
- Direct solar radiation in the Earth view (there is evidence of FOV contamination at night in the 3.7µm channel but less prevalent in the AVHHR/3).

A second effect relates to the "PRT representativeness (thermal gradients)" effect described above and is covered by that effects table (the uncertainty associated with thermal gradients will be larger for scanlines affected by solar contamination).

The reflected sunlight must, however, be considered separately for the 3.7µm channel. This is an effect that is under investigation, some comments are given in A.3.3. It should, however, be noted that the error introduced by the solar contamination is not the signal introduced by the solar radiation but is the error introduced by having to model the underlying gain variation for the periods where the solar radiance is significant. The effect will only affect the 3.7µm channel and so there is no correlation between channels. For this channel the effect will be common for the same time in successive orbits for orbits that are close in time. In this case the solar contamination is identical from orbit to orbit so there is going to be a close to 100% correlation for impacted scanlines. On longer timescales, there is evolution in where the solar contamination is seen which can be seen in the variations in the number of scan lines impacted. See appendix A3.3 for more details.

4.4.2 Effects tables for Solar contamination

Table 6 Effects tables for the IWCT band-integrated radiance due to solar contamination in the Earth view and due to the error in determining the IWCT temperature.

Table descriptor			
Name of effect		Solar contamination	IWCT temperature error
Affected term in measurement function		$\tilde{L}_{\mathrm{IWCT}}$	$\tilde{L}_{\mathrm{IWCT}}$
Instruments in the series affected		All	All
Correlation type and form	**Pixel-to-pixel [pixels]**	Rectangular Absolute	Rectangular Absolute
	from scanline to scanline	Truncated Gaussian	Truncated Gaussian

	[scanlines]		
	between images [images]	None	None
	Between orbits [orbit]	Rectangular Absolute	Unknown
	Over time [time]	Function of difference between number of scanlines impacted by effect	Function of difference between number of scanlines impacted by effect
Correlation scale	**Pixel-to-pixel [pixels]**	$[-\infty, +\infty]$	$[-\infty, +\infty]$
	from scanline to scanline [scanlines]	Function relating to solar contamination modelling.	Function relating to solar contamination modelling.
	between images [images]	None	None
	Between orbits [orbit]	100% correlation for impacted scanlines	None
	Over time [time]	Depends on the variation in the effect and will be modelled by looking at the observed characteristics	Depends on the variation in the effect and will be modelled by looking at the observed characteristics
Channels/ bands	**List of channels / bands affected**	3.7 μm only	3.7, 11 and 12 μm
	Correlation coefficient matrix	N/A	N/A
Uncertainty	**PDF shape**	Gaussian	Gaussian
	units	W m^{-2} sr^{-1}	W m^{-2} sr^{-1}
	magnitude	A model of the uncertainty will be provided	From gain bias adjustment
Sensitivity coefficient		$\dfrac{\partial L_{E}}{\partial L_{Solar}}$	$\dfrac{\partial L_{E}}{\partial T_{IWCT}}$

The sensitivity coefficients are not yet known or the exact nature of the error. We also do not have a complete estimate of the correlation structure but it will be something like 100% correlation for adjacent orbits for those scanlines with a detected solar contamination flag set since the solar contamination will be at the same point in the orbit with a very similar level. On longer timescales, the correlation between the errors will become less as the configuration of the satellite to Sun angle changes. This has both a yearly cycle and can have a longer-term component due to orbital drift. Examples of the time evolution of the number of scanlines is shown below and it is this sort of information which can be used to estimate the variation in the correlation coefficients on longer timescales. At the moment these long term correlation effects are not included in the FCDR.
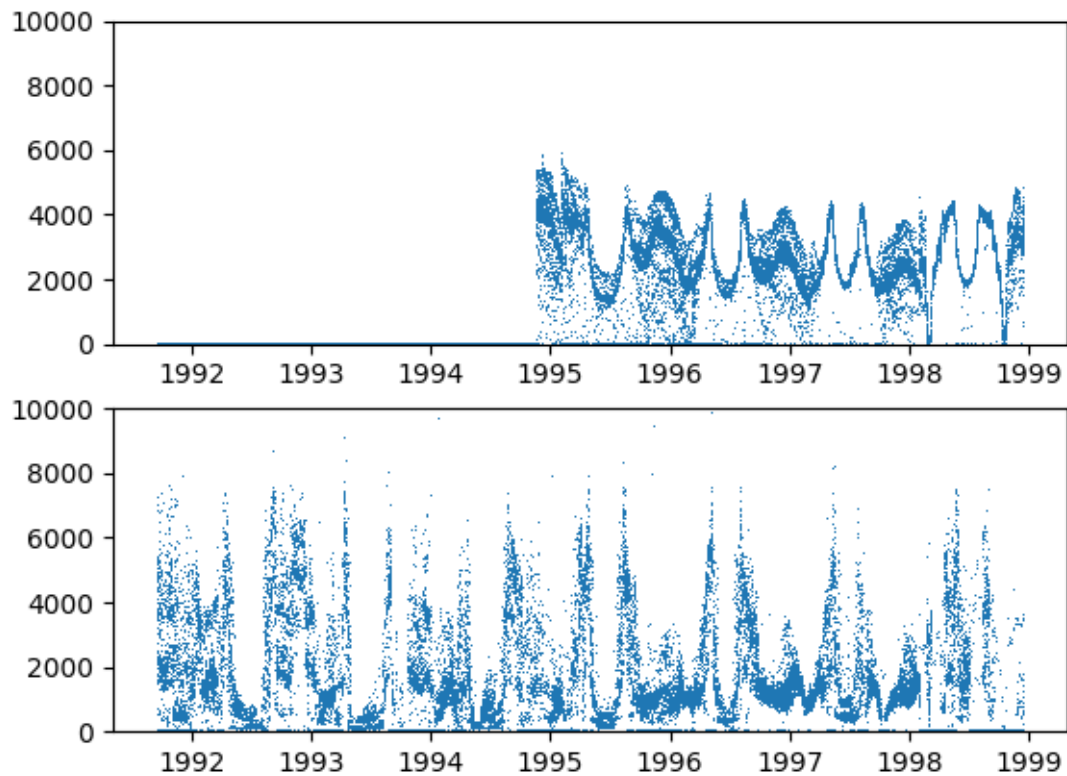
Figure 2 Number of solar contaminated scan lines detected per orbit for NOAA-12 using the operational (top panel) and new solar contamination algorithm (bottom panel). This shows the lack of solar contamination detection in the operational data before late 1994 but also shows the difference in the detection algorithms. This difference is, in part, due the new IWCT temperature error correction term also used in the new calibration which has removed some cases where the operational solar contamination algorithm erroneously removed data where the IWCT temperature error was large, mistaking it for solar contamination. It can be seen that the solar contamination in the new algorithm is much more strongly seasonal, unlike the operational case.

4.5   Thermal environment bias

One of the long term biases seen in the AVHRR is related to the overall thermal environment of the sensor and how that environment changes over time as the satellite orbit changes. First noticed in a characteristic SST bias seen relative to drifting buoys in NOAA-16 (Mittaz 2011b) the bias is strongly correlated with the IWCT temperature and seems best correlated when considering the orbital average of the IWCT temperature which we call the instrument temperature (T_{Instr}). It is, however, important the realise that T_{Instr} is actually only a crude indicator of the complex and variable thermal structure of the AVHRR instrument that is the true cause of the variable bias and therefore can only be thought of as a proxy measurement which is correlated to some extent with the true source of the bias. The physical origin of the bias is due to the different views (space view, IWCT view and Earth view) seeing different amounts of straylight from different parts of the sensor. Because the part of the sensor seen by the different views are going to be different and also will be at different temperatures, changes in the thermal structure of the AVHRR will results in variable amounts of straylight and hence give rise to a time variable bias.

Table 7 Effects tables for the thermal environment bias

Table descriptor		
Name of effect		Thermal environment bias
Affected term in measurement function		$f(T_{Instr})$
Instruments in the series affected		All
Correlation type and form	**Pixel-to-pixel [pixels]**	Rectangular Absolute
	from scanline to scanline [scanlines]	Rectangular Absolute
	between images [images]	N/A
	Between orbits [orbit]	Rectangular Absolute
	Over time [time]	Truncated gaussian
Correlation scale	**Pixel-to-pixel [pixels]**	$\left[-\infty, +\infty\right]$
	from scanline to scanline [scanlines]	Function relating to solar contamination modelling.
	between images [images]	N/A
	Between orbits [orbit]	For orbits close in time there will be a 100% correlation in the error (T_{Instr} won't change between close orbits). On daily timescales will be assessed from the curve of T_{Instr} as a function of time
	Over time [time]	Correlation will drop off over time with a typical sigma of a year
Channels/ bands	**List of channels / bands affected**	All IR channels
	Correlation coefficient matrix	N/A
Uncertainty	**PDF shape**	Gaussian
	units	W m^{-2} sr^{-1}
	magnitude	A model of the uncertainty will be provided based on the final statistics relative to a matchup dataset
Sensitivity coefficient		$\dfrac{\partial L_E}{\partial T_{instr}}$

Without a full thermal model of the AVHRR and also given that the number of temperature measurements available are small, especially for the early sensors where the IWCT temperature is pretty much the only temperature available, T_{Instr} is the only indicator as to thermal state that is available across all AVHRRs. We therefore attempt to model the thermal environment bias as a function of T_{Instr}. Previous studies (e.g. Mittaz et al. 2013) have shown that the form of the bias dependence can have a time dependence in that different time periods can have distinctly different

T_{Instr} vs bias behaviours so the model to describe the bias can be both complex and temporally variable. The plot below shows the sort of behaviour seen in the AVHRR/1 and AVHRR/2 sensors relative to an RTM reference where sometimes a linear model works, sometimes a more complex model is needed. For NOAA-14 three different separate models were needed which cover different time periods and are denoted in different colours (see Appendix A.5 for further details). In the current version of the FCDR a simpler linear model has been used as derived from the Harmonisation process which needs to be updated for future releases.
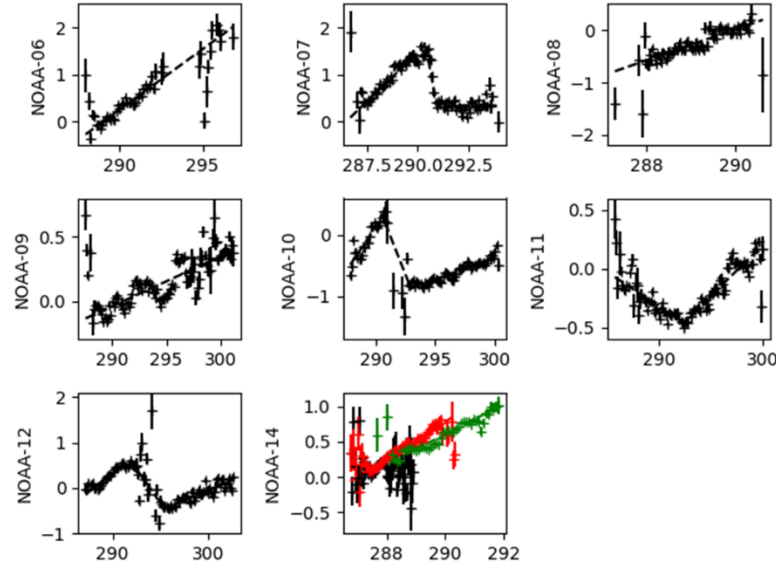
Figure 3 T_{Instr} versus bias (relative to an RTM modelled radiance) for a range of AVHRRs. Plotted is the T_{Instr} (x-axis) against bias (y-axis). The plots show the range of different behaviour seen across different AVHRRs. For NOAA-14 the different colours correspond to different time periods (see Appendix A.5 for more detail)

In terms of the correlation structure the current model calculated the bias on the basis of an orbital average temperature (note that the within an orbit bias terms are dealt with elsewhere). Therefore, within a single orbit there is just a single bias value and so all pixels have a 100% correlated error structure. On the timescale of one orbit to the next the value of T_{Instr} will not change significantly so again on the timescale of a day the correlation structure will be close to 100% but this can be assessed from timeseries of T_{Instr}. In the current FCDR the harmonisation model assumes a linear model only due to time constraints.

4.6 Emissivity

Note that there is no uncertainty associated with ε. This is because any error in this term will be corrected for by the harmonisation process.

4.7 Model assumptions

The +0 term in the measurement equation, Eq 3-2, considers the following effects:

- Non-quadratic nonlinearity
- Variable nonlinearity coefficient

The model equation assumes that the quadratic function fully describes the conversion from counts to radiance. For the HgCdTe detector (for the 11 μm and 12 μm channels), this may not be the case. Physically the nonlinearity is thought to be dominated by Auger recombination which is itself related to the lifetime of semiconductor carriers. As the total number of carriers changes, the Auger recombination rate changes and at higher carrier numbers suppresses the number of effective carriers

reducing the observed current. The exact details of the non-linear behaviour is then related to doping levels, lattice defects etc. in the detector and is not expected to be strictly quadratic. The first effect table is then to do with the non-quadratic nature of the nonlinearity. Because we cannot measure the effect in detail from the pre-launch measurements and we do not have access to the original manufactures data we cannot know exactly what errors may be introduced by assuming a simple quadratic. We are then left with a Type-B uncertainty estimate (expert judgement, see Appendix A.6).

The second effect table is related to the fact that the nonlinearity of an HgCdTe detector is not itself a constant even though the AVHRR measurement equation assumes that it is. Again, this is a case where there is experimental evidence of the variation in the nonlinearity (see for example Theocharous & Theocharous 2006) but for which estimates for the impact in the case of the detectors flown on-board the AVHRR sensors will be difficult if not impossible to directly measure. Again we have to use a Type-B estimate and cannot fold this effect into our measurement equation directly due to lack of information. This is described in more detail in Appendix A.6.

Table 8 Effects tables for the non-quadratic and variable nonlinearities

Table descriptor			
Name of effect		Non-quadratic nonlinearity	Variable nonlinearity coefficient
Affected term in measurement function		+0	+0
Instruments in the series affected		All	All
Correlation type and form	**Pixel-to-pixel [pixels]**	Rectangular Absolute	Rectangular Absolute
	from scanline to scanline [scanlines]	Rectangular Absolute	Rectangular Absolute
	between images [images]	N/A	N/A
	Between orbits [orbit]	Rectangular Absolute	Rectangular Absolute
	Over time [time]	Rectangular Absolute	Rectangular Absolute
Correlation scale	**Pixel-to-pixel [pixels]**	$[-\infty, +\infty]$	$[-\infty, +\infty]$
	from scanline to scanline [scanlines]	$[-\infty, +\infty]$	$[-\infty, +\infty]$
	between images [images]	N/A	N/A
	Between orbits [orbit]	$[-\infty, +\infty]$	$[-\infty, +\infty]$
	Over time [time]	$[-\infty, +\infty]$	$[-\infty, +\infty]$
Channels/ bands	**List of channels / bands affected**	11 µm, 12 µm	11 µm, 12 µm
	Correlation coefficient matrix	Diagonal matrix	Diagonal matrix
	Covariance		

Uncertainty	PDF shape	Gaussian	Gaussian
	units	W m^{-2} sr^{-1}	W m^{-2} sr^{-1}
	magnitude	Single value provided	Single value provided
Sensitivity coefficient		$\dfrac{\partial L_{\mathrm{E}}}{\partial L_{+0}} = 1$	$\dfrac{\partial L_{\mathrm{E}}}{\partial L_{+0}} = 1$

There is one further effect related to Analog-to-Digital Convertor (ADC) errors. Podestá et al (2003) and the NASA SST Pathfinder team first noted that for the 11µm channel of the AVHRR on NOAA-14 that there are 'holes' or gaps in their matchup database located at $1.3°C < T4 < 1.9°C$ for e.g. 1995 and at $2.4°C < T4 < 3.0°C$ for e.g. 1999. They attribute these gaps at cold temperatures to the ADC. The ADC converts continuous voltages from the radiometer into discrete values from 0 to 1023 (corresponding to a 10- bit digitization scheme) by successive approximation. A voltage fed into the ADC is compared to an initial threshold (defined by sensor electronics). If the input is greater than this threshold, the highest order bit is set *on*, otherwise the bit is *off*. Voltages above and below the initial threshold are then compared to a second layer of thresholds which define the status of the second highest order bit, and so on until all bits are resolved. If the thresholds in the ADC do not coincide with their nominal values (e.g., as a result of drift in the electronics), then some of the output digital values can be wrong (see Appendix A.4).

5   Harmonisation

Harmonisation across the sensor series for FIDUCEO project purposes is described separately, so only a brief overview is considered here. The harmonisation coefficients represent the nonlinearity of the instrument (note this is distinct from the nonlinearity of the detector itself due to nonlinearities in the electronics as well as nonlinearities introduced due to SRF issues), the bias due to straylight differences between the calibration and observation views and an emissivity correction respectively. Note the relevant harmonization parameters:

- a_0: as shown in Mittaz et al. (2009), this term arises from differences in the straylight between the Earth view position and the space view position.

- a_1: is a correction factor to the emissivity term. This is needed in part because the only value for the emissivity for the AVHRR was a theoretical estimate only. This terms also partially corrects for problems with variable gradients across the IWCT in an average sense (Mittaz et al. 2009).

- a_2: is a bias correction term for the radiance of the IWCT which we set to zero and model as part of the thermal environment bias model (see also a_4)

- a_3: is the instrument nonlinearity. This is caused both by the native nonlinearity of the detector as well as nonlinearities due to the on-board electronics. There will also be a component which will partially correct for differences between the assumed and true spectral response function.

- a_4: a harmonization term needed to align the thermal environment bias model with the true instrument behaviour (see also a_2). Note that in the current version of the FCDR the function is a linear term in T_{instr}.

The harmonisation process will determine these parameters, and a covariance matrix for the parameters. To propagate these uncertainties through to the uncertainty associated with the Earth radiance we need the sensitivity coefficients:

$$\frac{\partial L_E}{\partial a_0} = 1 \qquad\qquad Eq\ 5\text{-}1$$

$$\frac{\partial L_E}{\partial a_1} = \frac{\tilde{L}_{IWCT}\left(\bar{C}_S - C_E\right)}{\left(\bar{C}_S - \bar{C}_{IWCT}\right)} \qquad\qquad Eq\ 5\text{-}2$$

$$\frac{\partial L_E}{\partial a_2} = \frac{-\left(\bar{C}_S - C_E\right)}{\left(\bar{C}_S - \bar{C}_{IWCT}\right)} \qquad\qquad Eq\ 5\text{-}3$$

$$\frac{\partial L_E}{\partial a_3} = -\left(\bar{C}_S - \bar{C}_{IWCT}\right)\left(\bar{C}_S - C_E\right) + \left(\bar{C}_S - C_E\right)^2 \qquad\qquad Eq\ 5\text{-}4$$

$$\frac{\partial L_E}{\partial a_4} = f\left(T_{inst}\right) \qquad\qquad Eq\ 5\text{-}5$$

where T_{inst} is a z-score obtained by normalizing using the mean and standard deviation of the orbital temperature associated with each sensor.

Note that the harmonisation coefficients will be correlated with each other and the result of the harmonisation process generates a covariance matrix for these. Therefore to propagate uncertainties, the full law of propagation of uncertainties, including the correlation term, is required. Note that the harmonisation coefficients will be the same for all time with one sensor and there will be a correlation between different sensors in the FCDR series because of correlations between harmonisation coefficients over these longer timescales.

A   Appendix on detailed information about uncertainty components

A.1   Noise and cross talk, correlations observed

Noise can arise in a number of different physical process. There will be noise from the detector itself which can be related to a range of physical causes including but not limited to thermal noise (itself related to the detector temperature), shot noise (related to the number of photons hitting the detector at any one time) etc. There will also be noise from the electronics which often will have a characteristic noise spectrum of *1/f*. And there can also be cross-talk where either an extraneous signal is introduced into the observed signal or one channels signal can cross over and contaminate another channel. This latter effect will give rise to correlations between channels.

In the case of the AVHRR all of the above effects have been seen, In particular the 3.7µm channel has shown a strong time dependent noise term which has a noise spectrum close to *1/f* (e.g. Mittaz 2016). This indicates that much of the noise in the 3.7µm channel arises in the electronics and there is further support for this from the AVHRR on TIROS-N. In the case of TIROS-N it has been known since it was launched that the noise was highly variable within an orbit and this was fixed in subsequent AVHRRs by changing the design of the electronics. TIROS-N also shows evidence for a strong cross-talk signal which again was significantly reduced when the electronics was re-designed.

To measure the noise for all channels we have first removed the many outliers that can occur. At the moment the outlier information is based on simple thresholds followed by an outlier rejection based on a mean/standard deviation estimate in a running window. The algorithm works well as will be shown below. The thresholding has a significant impact on both the measured signal as well as the noise estimates (see below). We have used the Allan deviation to generate the statistics as this allows us to calculate the noise for both space and IWCT views in the same way (for more details see Mittaz 2016).

A.1.1   Visible channels

While we are not recalibrating the visible channels we are including them in our FCDR so they need uncertainty estimates. Because we are not recalibrating these channels we cannot do a full uncertainty analysis but we can include some components of the uncertainty. First is the Allan deviation from an orbits worth of data which represents the uncertainty caused by random effects. Second is an uncertainty on the averaged space counts (structured uncertainty). Third is a common component of uncertainty related to the uncertainties in the calibration coefficients used to generate the visible channel data which is based on the visible channel coefficients taken from the CSPP (Community Satellite Processing Package) package which is itself based on the PATMOS-X calibration (e.g. Heidinger et al. 2010). Note that the visible channels do not have any on-board calibration system so the updates to the calibration are done vicariously.

Figure 4 shows both the noise and mean values of the space (dark) counts for the 0.6µm channel on NOAA-09 and shows both the importance of filtering on both the noise and mean estimates as well as the fact that the noise itself is time variable. These estimates are included in the FIDUCEO FCDR. Also included are uncertainties due using an average estimate of the space counts which will have a correlation length scale of the order of the smoothing kernel.

For the uncertainty due to common effects this will be based on estimates of the uncertainty of the visible channel calibration process. The quoted estimates from Heidinger et al. (2010) are 2%,3% and 3% for the 0.6µm, 0.8µm and 1.6µm channels. However, a preliminary analysis of the difference

between multiple versions of the PATMOS-X calibration as well as compared to another independent estimate from NASA (NASA LaRC FCDR Doelling, D., Minnis, P., and the NOAA CDR Program (2015)) shows differences of the order of 3%, 5% and 5% (sometimes much larger) so we will be using these updated estimates of the uncertainty for the non-random component of uncertainty in the easy FCDR.
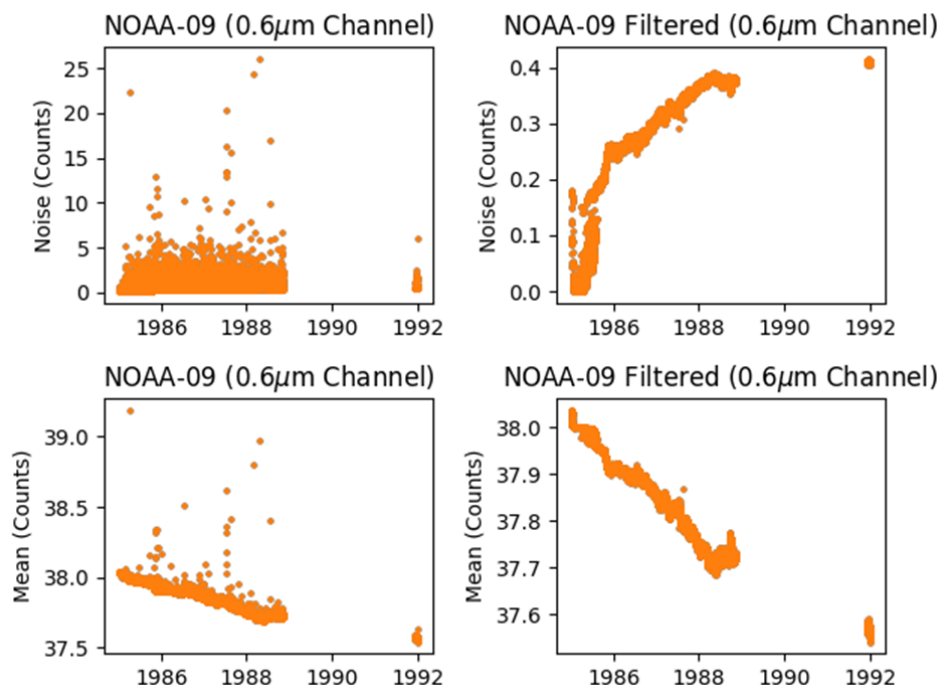

Figure 4 Noise and mean counts from NOAA-09 0.6 micron channel. The left hand column shows the estimated noise and mean value before filtering and the right hand column shows the same after filtering. So both a filtered dataset and a variable noise are needed to correctly use the AVHRR visible channel data.

A.1.2 IR Channels

The filtering and noise estimates are the same for the IR channels. Again we see time dependent variations and also note the importance of filtering on the data. Figure 5 shows an example for NOAA-07 where the noise increases to a large value for the 3.7µm channel and then drops back down abruptly at the end of September 1983. At this point the instrument was outgassed and the IR sensors were turned off effectively resetting everything. This behaviour therefore indicates that the noise is not dependent on the physical state of the detector or of the incident flux levels but is related to something else on-board such as the electronics. This is also supported by the fact that for the AVHRR/3 sensors the electronics were redesigned and similar noise patterns were not seen. As for other sensors as stated above, TIROS-N is a special case as the noise varied significantly around the orbit with something approximating to a day/night variation.
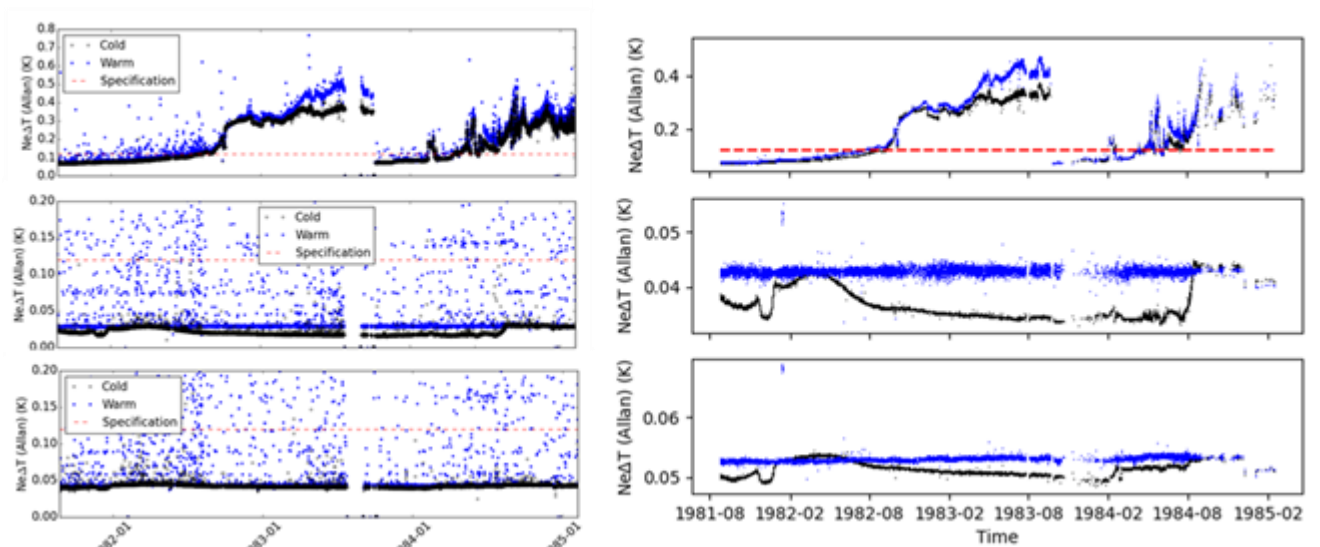
Figure 5 Space view (black) and ICWT noise (blue) estimates for NOAA-07. The left hand column shows the pre-filtered data, the right hand column shows the data after filtering. The red dotted line is the pre-flight specification. The 3.7µm channel noise (top panels) is highly variable with a step jump seen in late 1983. This was caused by an outgassing event that turned off the IR channels for an extended period and illustrates how the noise is not just from the detector but is influenced by the electronics/spacecraft as well. The 11 µm channel noise (middle panel) and the 12 µm channel noise (lower panel) are more stable.

In terms of noise covariance across the channels and scanning positions, for the space view and for the ICT, some evidence of cross-talk has been found in the older instruments in the sensor series. In Figure 6, the correlation with scanline position for the space view shows strong correlation with neighbouring scanline positions in the case of Channel 3b of TIROS-N. For IR channels 4 and 5, there is strong cross-talk in the first five positions. The older NOAA-07 also presents cross-talk (albeit with some block structure) in the space view in channel 3b but channels 4 and 5 do not show any strong cross-talk effect.

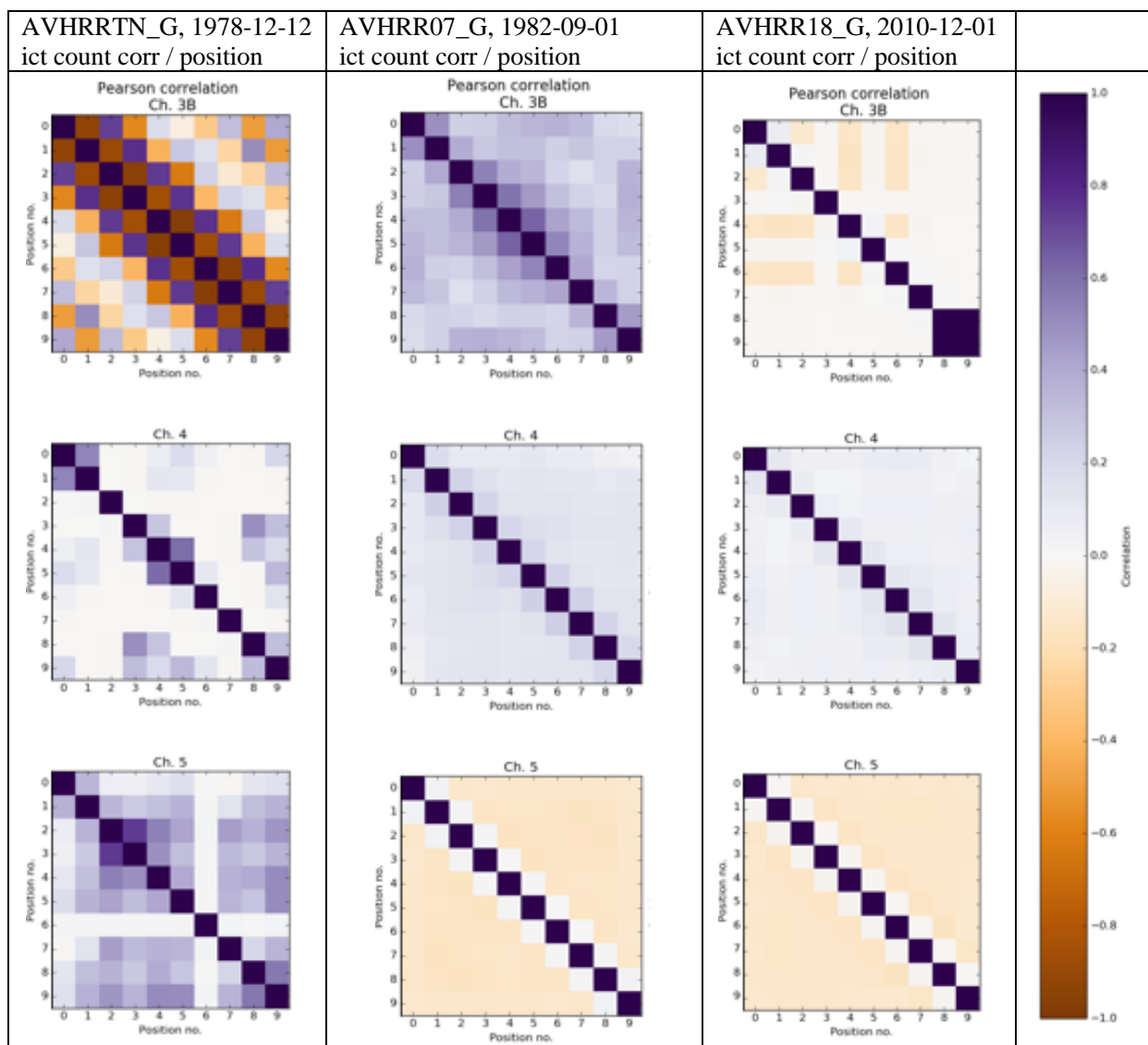| AVHRRTN_G, 1978-12-12 space count corr / position	AVHRR07_G, 1982-09-01 space count corr / position	AVHRR18_G, 2010-12-01 space count corr / position	
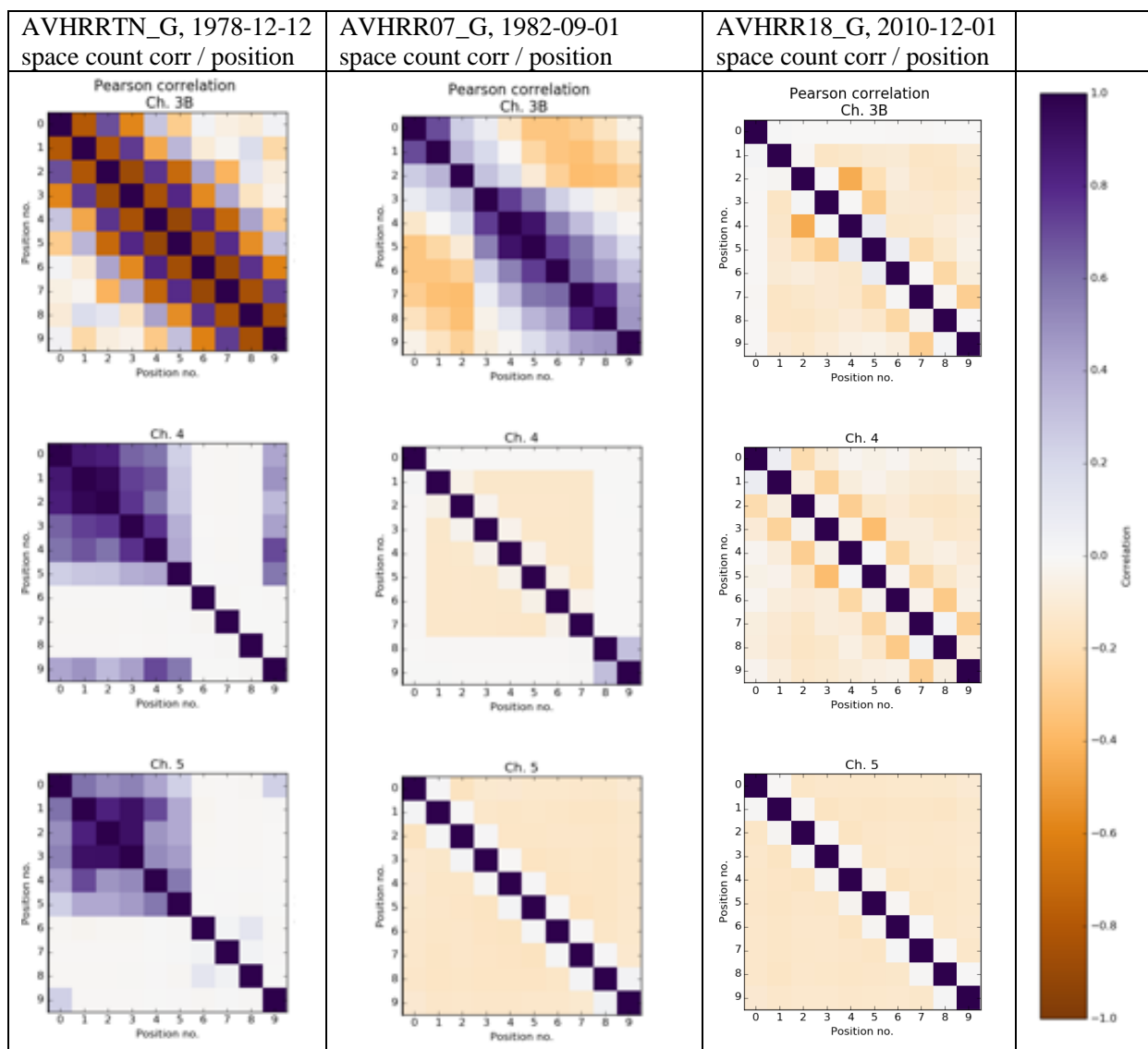
Figure 6 Space view noise correlations between reflectance channels for TIROS-N, NOAA-07 and NOAA-18. The Pearson product-moment correlation is shown.

A similar picture is painted by ICT noise correlations with scanline position in Figure 7. Strong cross-talk is evident for TIROS-N on channel 3b. Some localized cross-talk and a block structure is observable for channel 5 (channel 4 looks more free of cross-talk). NOAA-07 and NOAA-18 exhibit similar phenomenology to the space view case with correlations across scanline positions in the case of channel 3b and little or no evidence of cross-talk in channels 4 and 5.

AVHRRTN_G, 1978-12-12 ict count corr / position	AVHRR07_G, 1982-09-01 ict count corr / position	AVHRR18_G, 2010-12-01 ict count corr / position	

Figure 7 ICT noise correlations between reflectance channels for TIROS-N, NOAA-07 and NOAA-18. The Pearson product-moment correlation is shown.

This suggests that the cross-talk issue has been addressed in the sensor series post-1982 especially for the two IR channels 4 and 5. Note, the cross-talk term has not been included in the current FCDR.

A.2 Spectral response function biases

The errors caused by spectral response differences have yet to be included in our current FCDR but will be studied in the future. With the current work there will be some correction for possible SRF errors because as already mentioned, the nonlinearity term in the harmonisation (a_3) will correct for some SRF problems.

A.3 Internal warm calibration target (IWCT) effects

A.3.1 PRT noise

Within FIDUCEO, we have performed a detailed study of the PRT noise which appears to be constant over time and for all versions of the AVHRR. Its value is close to 0.3 counts or 0.015 K as can be seen in Figure 8 for NOAA-07 below.
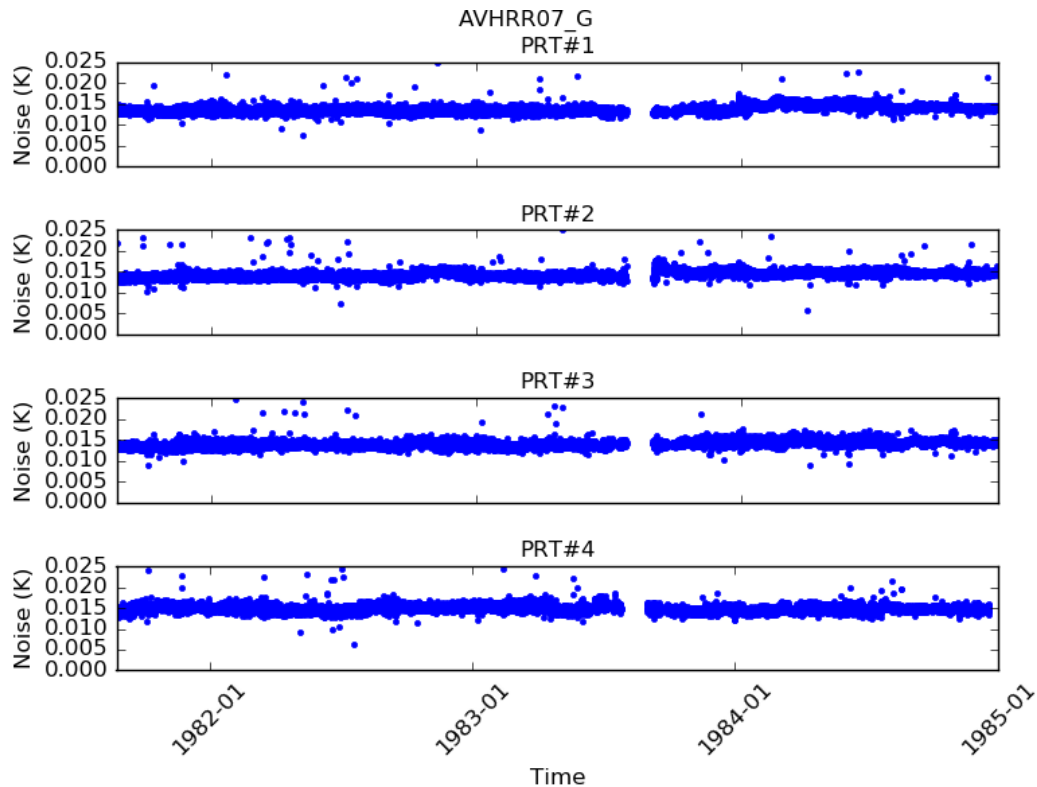
Figure 8 Noise of the four individuals PRT for NOAA-07, in temperature. The noise is estimated by calculating the Allan deviation of all the PRT measurements over an orbit.

A.3.2 Thermal gradients across the IWCT

Because the IWCT on the AVHRR is not a sophisticated blackbody and should rather be seen as observing a portion of the instrument blackbody, other effects come into play. Thermal gradients across the IWCT are not controlled and only four PRTs were used to measure its temperature (which is insufficient to reliably detect complex thermal gradients across its surface if present). This means that lack of knowledge of such gradients will give rise to an uncertainty on the final IWCT radiance.

An estimate of the size of such non-uniformities can be made if we assume that the PRTs are equidistant from each other. We can then fit a simple plane to three of the PRT temperatures and see if the fourth is consistent with the other three. If it is, then gradients across the IWCT are not a problem. Figure 9 shows that the distribution of the difference between the measured PRT temperature and the PRT temperature deduced from the 3 others, for three days selected to represent three different epochs of AVHRR behaviour. It is apparent from Figure 9 that not only it is likely that an assumption of a uniform temperature gradient across the IWCT is wrong, but that there is also a time-dependent component.
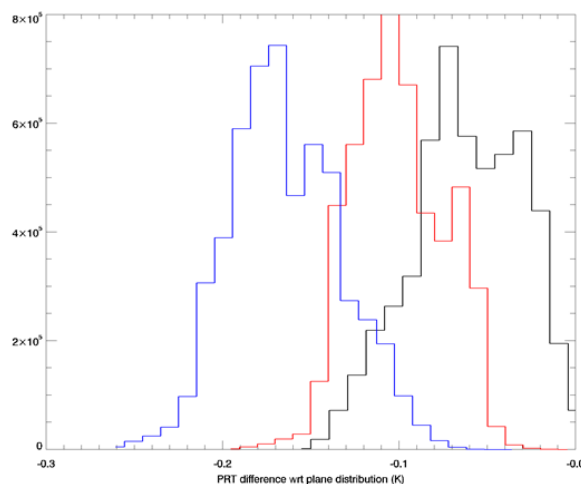
33

Figure 9 Difference between a planar temperature distribution over the ICT and a measured value for three epochs (01-01-2003, 01-01-2004 and 01-01-2009) for NOAA-16. Not only is the assumption of a planar distribution not met, but the average gradient also change

Furthermore, the IWCT error arising from such gradients applies to all IR channels. While such gradients also appear in other instruments and their impact is time dependent and related to orbit drift, this will need assessing for all sensors with on-board calibration. The uncertainty arises because the IWCT is subject to large (>1 K) time-variable thermal gradients and, as a result, the relationship between the true IWCT radiant temperature and these four point temperature measurements is not simple. Four PRT temperatures are inadequate to determine much detail about the complex thermal gradients across the surface of the IWCT. We can, however, exploit understanding of the behaviour of the 3.7 μm channel to constrain the problem. This channel uses an InSb detector which is known to be linear for the radiance levels observed from Earth observation. The 3.7 μm channel gain is therefore expected to be constant around the orbit. We can then reasonably infer that significant deviations from a constant gain reflect errors in the IWCT temperature estimate (Mittaz, Merchant and Woolliams, 2019). A direct mapping from gain error to IWCT temperature error constrained by the PRT measurements themselves can then be made (full details of the procedure will be published elsewhere but see Appendix A.6 for an example). This effect has never previously been characterised for the AVHRR. The effect table for the error in determination of the IWCT temperature is shown as Table 6. We note that currently for the AVHRR one of the table entries (correlation type and form between images/orbits) is labelled as 'Unknown' because we do not currently know what this is apart from a general statement that we might expect close in time orbits to have similar correlation structures and those far apart in time having less correlation.

To get a feeling for the correlation scale associated with modelling the thermal gradient with a planar model, we calculated the anomaly between the measured value of PRT4 and the expected value from a linear fit through the other 3 PRTs for a range of cases. In particular, we investigated the variation of the PRT anomaly along scanlines and across orbit (i.e. on various temporal scales) for the AVHRR/3 sensor onboard NOAA-18, and also for the AVHRR/1 sensor onboard NOAA-8 and the AVHRR/2 sensor onboard NOAA-7. This choice caters for both morning and afternoon equatorial crossings, and also allows for a comparison of the AVHRR/3 sensor that has implemented a sun shield.

In order to ensure consistency between plots, we used the Haversine formula for great circles on a spherical Earth and integrated the central angle with respect to equatorial crossing time. This 'distance' measured in angular radians is invariant in the time domain and is calculated directly from geolocation via the latitudinal and longitudinal coordinates.

For each sensor we have selected a baseline day and calculated the PRT anomaly for all scans that day to 1) assess the typical variability and hence potential correlation structure along a scanline and 2) to assess correlation with neighbouring scanlines. We then also selected orbits at approximately midnight on different days at the daily, monthly, yearly and multi-year timescale. Figure 10 presents the results of this sampling approach across the 3 generations of the AVHRR using the aforementioned sensors.
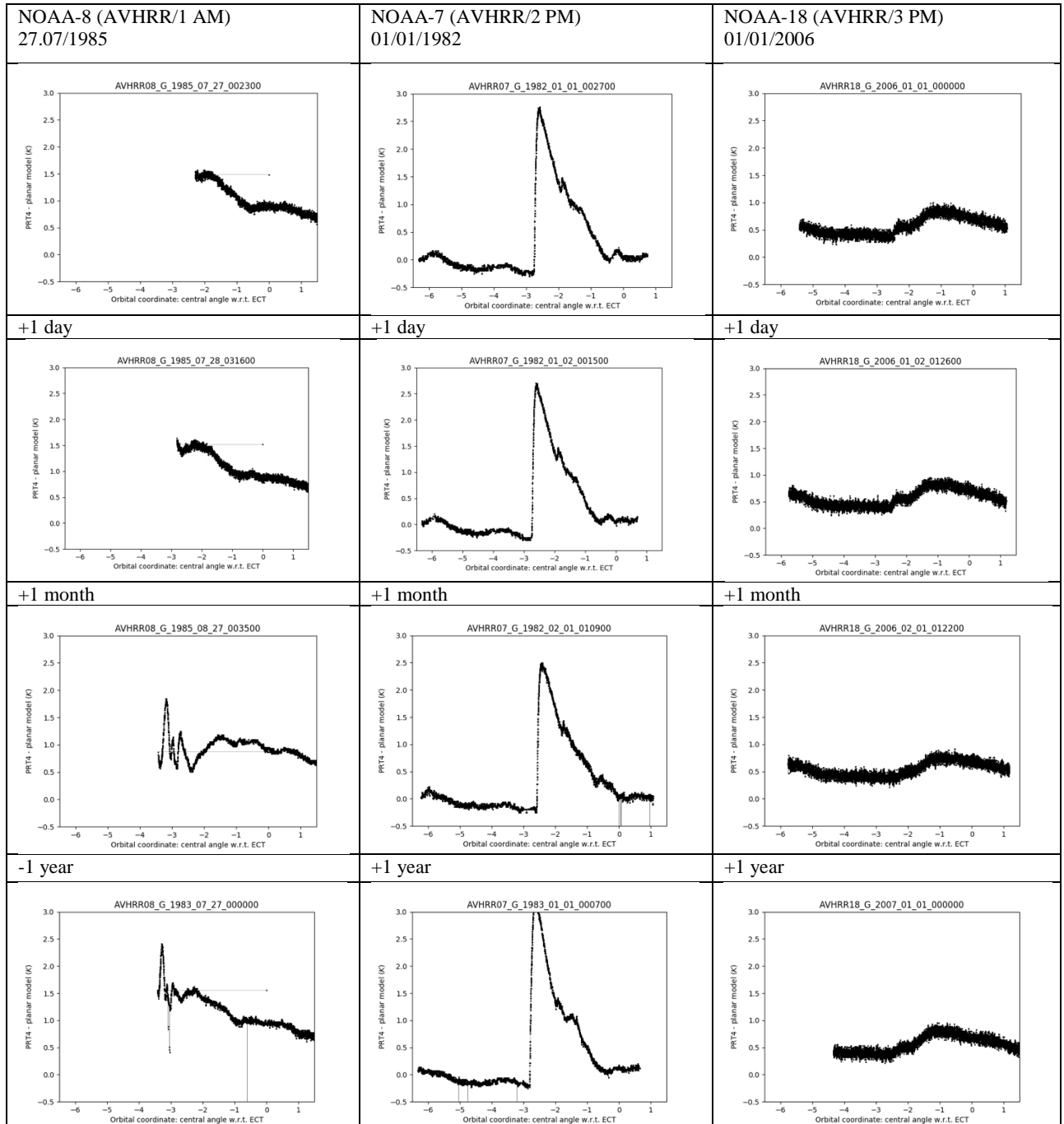

Figure 10 Variation of the PRT4-planar model scanline anomaly for the AVHRR/3 sensor NOAA-18 and the non-AVHRR/3 sensors NOAA-8 and NOAA-7 over a range of temporal lags with respect to the first scanline plot.

Very different correlation structures can be observed for the AVHRR/1, AVHRR/2 and AVHRR/3 sensors. On 27 July 1985, the AVHRR/1 sensor onboard NOAA-8 presents a scanline PRT4–planar

model anomaly structure that is similar on the daily scale but shows strong variability a month later. The total variability along the scanline is of the order of 1-1.5K. One year on, the behavior is starting to bear closer resemblance again to the initial case suggestive perhaps of an annual cycle.

In the case of the AVHRR/2, solar contamination leads to a change in anomaly of the order of 1.5-2.0K over all scales but either side in a 1-hr temporal interval, approximately constant anomaly is observed. We interpret these flat near-zero regions as indicative of the planar assumption being valid there. Contrary to AVHRR/1, the PRT anomaly structure shows strong resemblance up to the yearly timescale – suggestive of a longer-term correlation structure for this sensor. We will quantify this stable correlation structure (that is present both in neighbouring scanlines and across-orbits for the AVHRR/2) and provide a function for the correlation scales involved.

Very different anomaly time series are observed in the case of the AVHRR/3 sensor that has a sun shield in place. The traces appear broadly more sinusoidal in form and there is little or no visual evidence of strong solar contamination. This is true over neighbouring scanlines and over the multiple timescales considered here. In the AVHRR/3 plots the scanline anomaly also appears to be somewhat lower in magnitude.

A.3.3   Solar contamination

At the moment the operational gain calculation (for the 3.7 μm channel) identifies peaks in the gain due to sunlight reflected off the ICT and "chops them off" using a detection and fitting procedure that has been applied since November 1995. Figure 11 shows an example of the implementation of this method to the 3.7 μm channel of NOAA-14. There is an uncertainty associated with this correction related to the interpolation across the filtered section of the time series into the region of the tail of detected peaks.
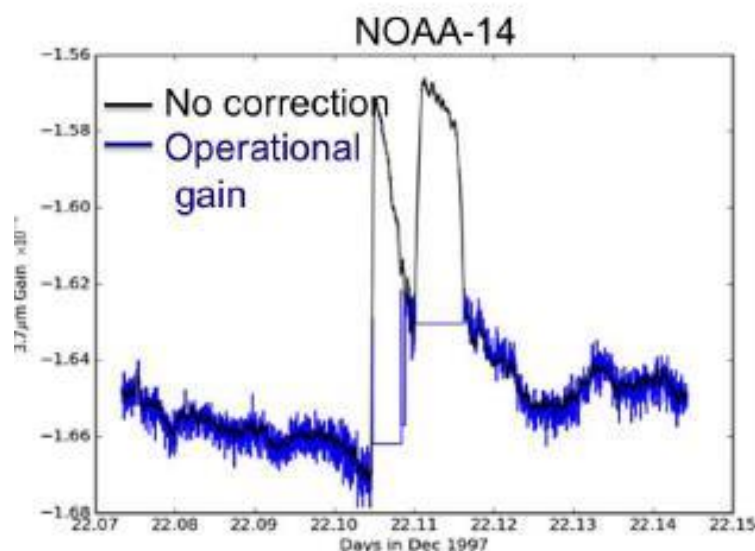

Figure 11 Detection of a solar contamination event in the 3.7 μm channel of NOAA-14 and the corrected operational gain obtained by interpolation of the filtered signal. Note that this procedure introduces an uncertainty associated with interpolation across filtered portions of the time series into the region of the tail of each peak.

There are two improvements that are planned to reduce the impact of the solar contamination. The first is to have a new solar contamination detection algorithm which would be similar to the current operational algorithm shown in Figure 11. This is needed because operationally the detection of solar

contamination effects was only introduced in 1994 which means that all the early AVHRRs have had no solar contamination detection applied at all. The introduction of the operational algorithm is clearly shown in Figure 2.
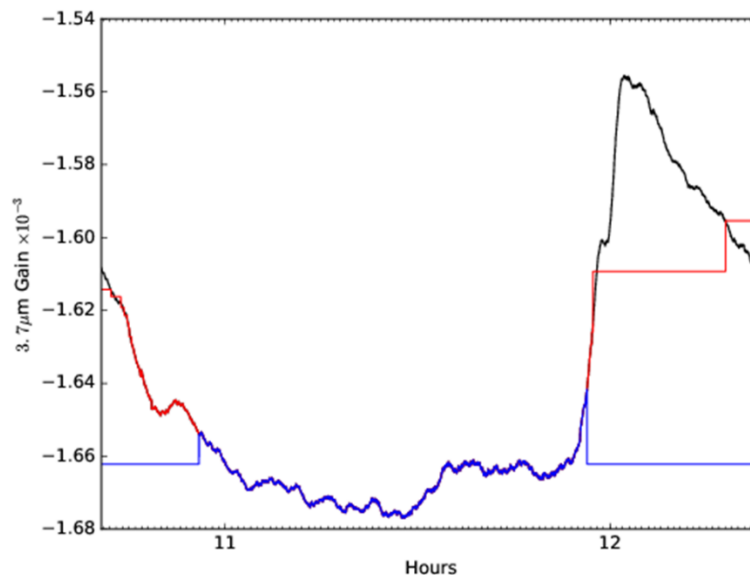

Figure 12 One orbit for NOAA-12 showing the new algorithm (in blue) detects more of the solar contamination event than the operational algorithm (in red). In this case half the orbit is actually impacted by the solar contamination.

Figure 12 shows the difference between the new and old algorithm at the orbit level. The blue line shows the new algorithm and the red the old and it can be seen that the old algorithm misses a lot of the apparent solar contamination. Therefore the new algorithm works both for the pre-1995 data as well as being an improvement over the old algorithm when present.

A.4 Analog-to-Digital Converter errors

The AVHRR uses a digitizing scheme where high counts correspond to low brightness temperatures. Thus, low SSTs at high latitudes are predominately affected because the high- order bit is set to on for these conditions, whereas temperate and tropical SSTs are potentially affected by less apparent problems in the low order bits. SST fields apparently are affected between 2 and 6°C, and values may be systematically over- or under- predicted by as much as 0.5°C (Podestá et al., 2003). We have checked all AVHRR/1 and AVHRR/2 data for this effect and we observe prevalent ADC drop-out for the 11µm channel not only at 511 counts but also at 769 counts at temperatures colder than SST.
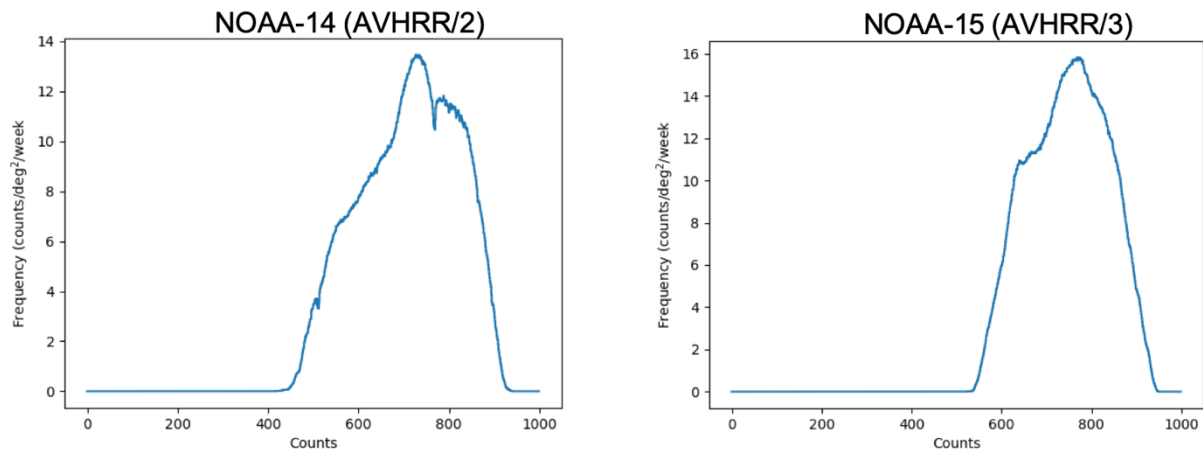
Figure 13. Left: the drop-out at 511 and 769 for the AVHRR/2 on NOAA-14. Right: the more expected behaviour for the AVHRR/3 on NOAA-15.

The error is related to problems in registering the right count at the lowest steps of the ADC and, because the AVHRR has inverted counts (high count = low radiance), this forces large steps between errors. In a normal count regime the impact counts will be close together and so this will look more like noise. A change in electronics design for the ADC fixed this for AVHRR/3. In the product user guide (PUG) accompanying the FCDR, we provide warnings regarding certain BT ranges.

A.5   Thermal environment bias effects

Figure 15 shows data for NOAA-12. The left hand plot shows the original and corrected 3.7 μm channel gain. The right-hand plot shows the IWCT temperature estimates made using the simple mean of the PRTs (original) and corrected by analysing the 3.7 μm channel gain. The corrected gain has lower variance, suggesting a substantial reduction in the IWCT temperature error and the remaining variability in the 3.7 μm channel gain can be used to estimate the IWCT temperature uncertainty. The improved IWCT temperature can then also be used to calibrate the 11 μm and 12 μm channels, where constant gain is not expected. This metrological approach estimates IWCT temperature with reduced systematic errors, and provides a method to evaluate the remaining uncertainty, for propagation to uncertainty in measured radiances. This effect is also one that will introduce channel-to-channel error correlation because any remaining error in the IWCT temperature will be present in the calibration of all the infrared channels.
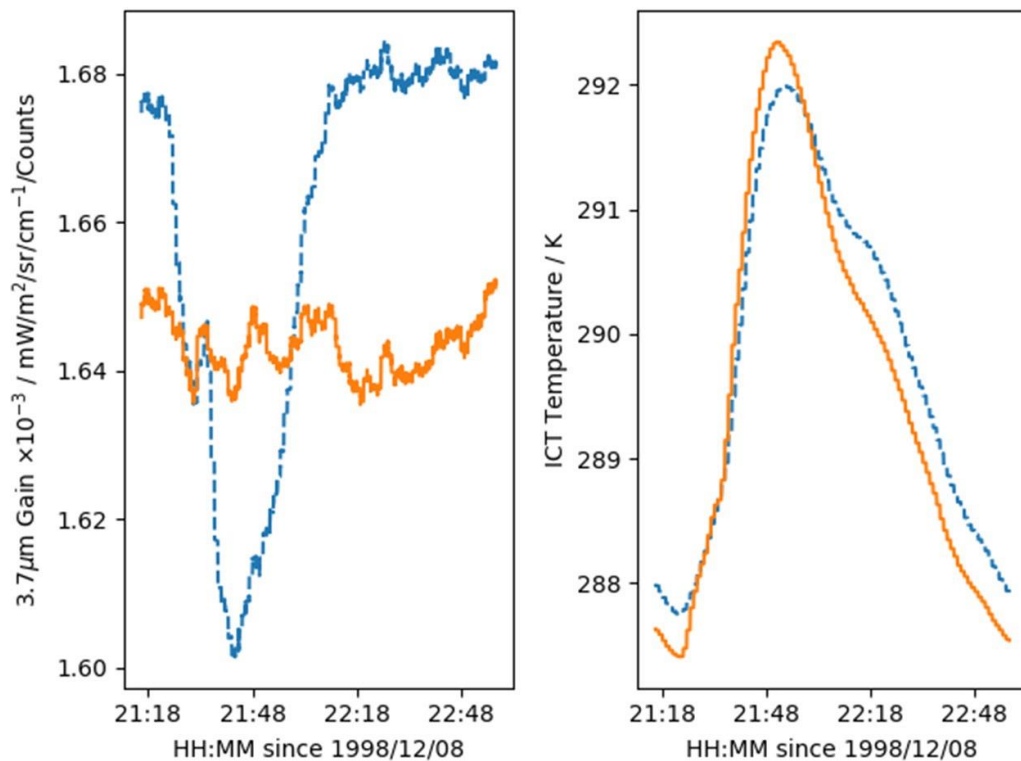
Figure 14. Left: the uncorrected (dashed) and corrected (solid) gain of the 3.7 µm channel as a function of time. Right: operational (dashed) and corrected (solid) estimate of the IWCT temperature. The properties of the 3.7 µm channel are such that there should be no gain variation, so the excursion seen in the uncorrected gain (left panel, blue) points to the IWCT temperature being mis-estimated (right panel, blue). After applying a method that re-estimates the IWCT temperature while minimising the variance of the 3.7 µm channel gain (left panel, orange), the corrected IWCT temperature variation (right panel, blue) can be used to remove bias in the other channels (11 and 12 µm) that depend on the IWCT temperature for their calibration.

From Mittaz et al. (2009) it is known that the a_0 term in the measurement equation can be shown to be related to the difference between the straylight components present when looking at the Earth view and the space view. This then directly relates the original a_0 term to the thermal state of the AVHRR since the stray light will originate from certain (unknown) parts of the instrument body/optical train. Looking at it this way it is then clear that if the thermal environment of the AVHRR changes then the value of a_0 will also change. Given that there are long term changes in the Earth-Sun distance as well as in the AVHRR orbit itself (apart from the MetOp versions) we then expect a change in the AVHRR thermal state on long timescales.

We can see this by looking at the orbital average of IWCT temperature as a function of time. Figure 13 shows this for the AVHRR/3 sensors and shows a wide range of variability from NOAA-15 which for its whole life was subject to large temperature variations to NOAA-16 which shows distinct phases of variability to MetOp-A which shows small annular variations. The coloured lines at the top of some of the plots show where different time ranges have been defined for different models of the bias caused by the changes in the thermal environment. That different models are needed can be seen in Figure 16 where the bias between the NOAA-16 AVHRR and the AATSR sensors are shown for different time periods (the red and green times shown in Figure 13).
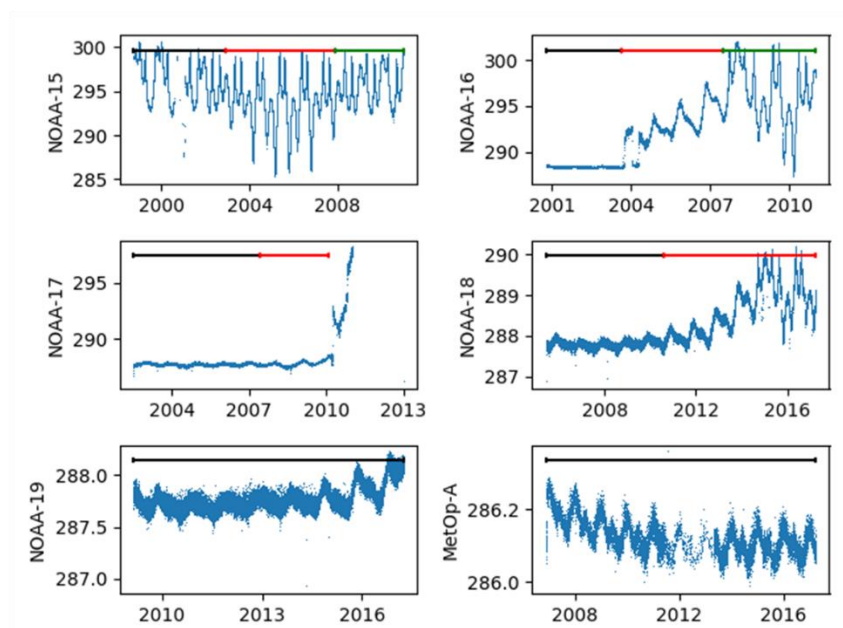
Figure 135 The time variability of the orbital average temperature for the AVHRR/3 sensors. Note that there is a lot of variability which even includes MetOp-A which still shows an annual signal.
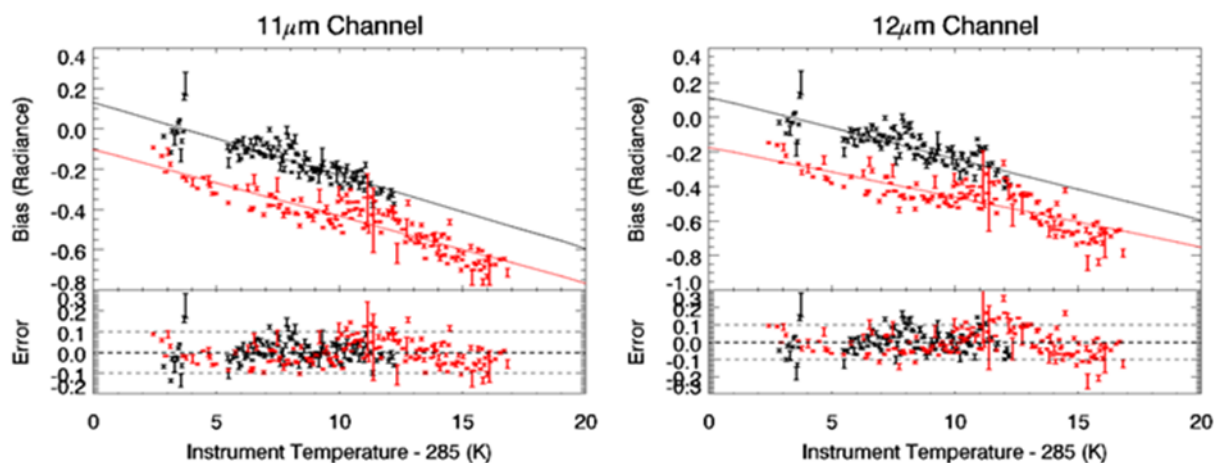

Figure 146 Bias of NOAA-16 AVHRR vs the AATSR for two time periods defined by the red (the black symbols) and the green (red symbols) lines in Figure 16. The separation in both the 11μm and 12μm channels shows the need for two different models

While in the current Easy FCDR we use a simple linear model we are investigating simple parameterisations of the instrument temperature vs bias dependence that are more complex than just a linear model. Versions are shown in Figure 3 for the AVHRR/1 and AVHRR/2 sensors and in Figure 15 for the AVHRR/3 sensors. In both plots the colours where present refer to different time zones. An estimate of the uncertainty in the model could be based on the statistics seen when deriving the model itself, and there would be an extra uncertainty added though the harmonsation process. This more complex modelling will be added into later versions of the FCDR.
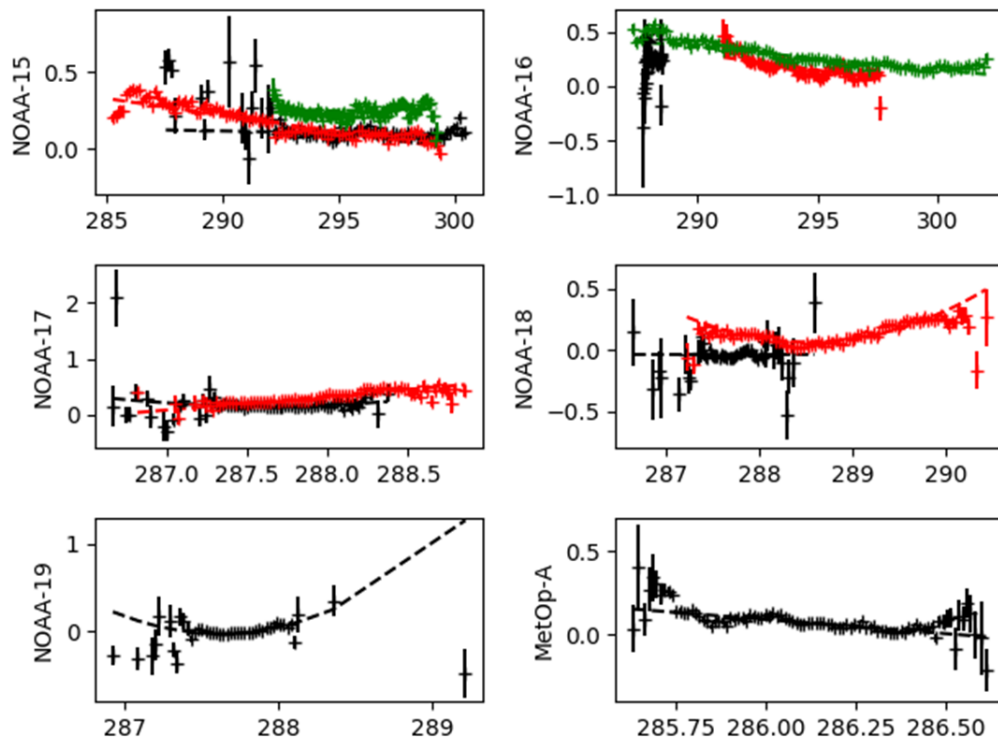
Figure 157 Thermal environment bias (relative to RTM BTs) as a function of the instrument temperature for the AVHRR/3 sensors.

A.6 Model assumption effects

Table 6 presents two model assumption effects. The first is related to the non-quadratic nature of the nonlinearity and the second to the variability of the nonlinearity coefficient. Estimates of the scale of both effects have been derived from a numerical model of an HgCdTe detector based one used for the GOES Imager detectors (Bicknell 2000). The model determines the Auger recombination lifetimes of the carriers and hence variations in the predicted voltage seen for a given input photon flux and has been tuned to match the sort of photon fluxes and non-linearities seen in the AVHRR sensors. The top two plots of Figure 16 show the predicted deviation of the estimated brightness temperature using a quadratic measurement equation compared to the input brightness temperature and indicates that the quadratic assumption may be introducing and error of order a few milli-Kelvin, at least in terms of modelling the Auger recombination effect.
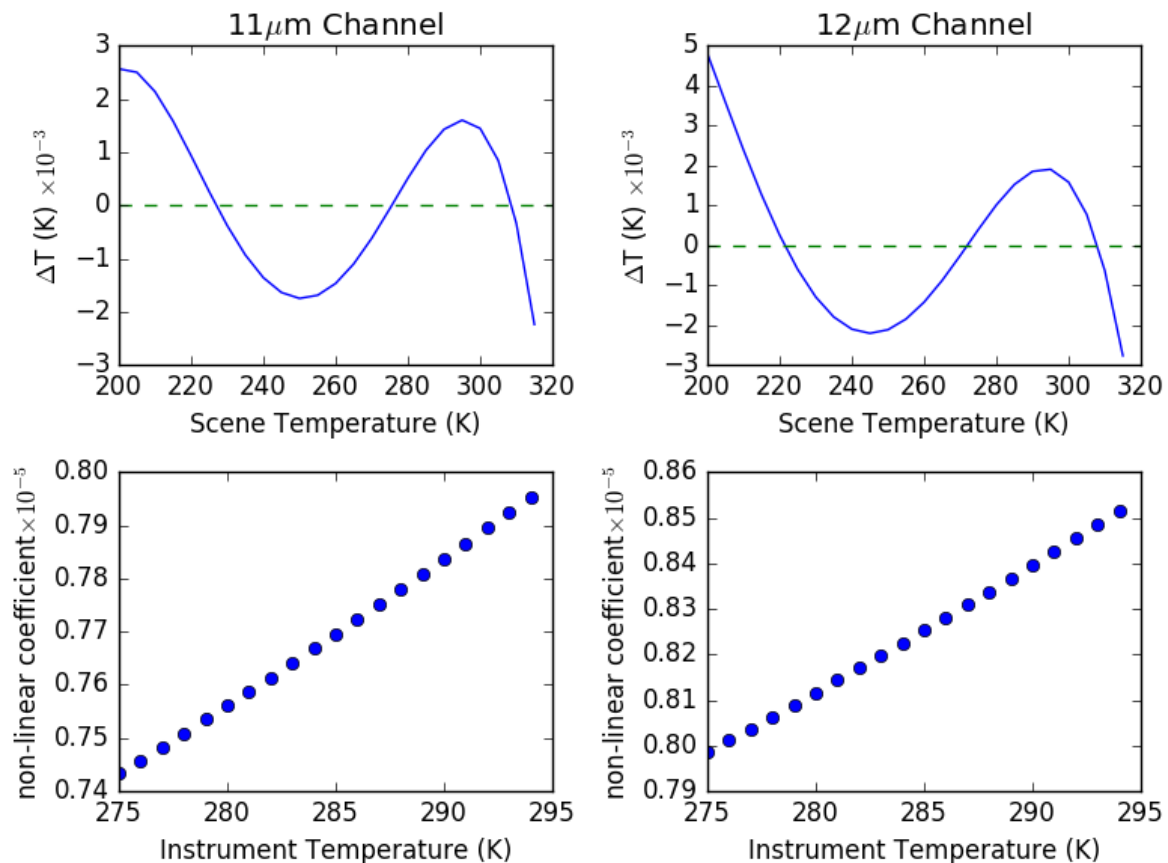
Figure 168 Top two plots show the deviation from a quadratic model for an HgCdTe detector for the 11 and 12μm channels using a theoretical model. This indicates that the deviation from a quadratic are at the milli-Kelvin level. The two lower plots show changes in the quadratic nonlinearity coefficient as a function of instrument temperature (a proxy for the total self-emission radiance) and indicates for a typical AVHRR orbit a variation of ~1% change in the coefficient.

The other nonlinearity effect that can be investigated using this model is the effect of the variable non-linear coefficient. To do this we have varied the self-emission component (parameterized by the instrument temperature) and tracked how the best fit quadratic term varies. This variation is shown in the lower panels of Figure 16 and shows over a 20 K variation in instrument temperature a variation of order 5% in the quadratic term. Given that a typical AVHRR shows orbital temperature variations more like ±1 degree this amounts to an approximately 0.4% change in the non-linear coefficient. For a 300K scene temperature and a typical instrument gain and nonlinearity this would correspond to an error of approximately ±0.006K which is of order the same size as shown for the non-quadratic error.

Both estimates are included as part of the uncertainty budget of the final FCDR.

A.7 Measurement equation and Harmonisation parameters

The measurement equation currently used for the Easy FCDR is a modified version of Eq 3-2, where a_2 has been set to zero and $f(T_{Instr}) = (T_{Instr} - T_{mean})/\sigma_{T_{Instr}}$ where T_{Instr} is the orbital average IWCT temperature, T_{mean} is the mean T_{Instr} over a sensors lifetime and $\sigma_{T_{Instr}}$ is the standard deviation of T_{Instr} again over the sensors lifetime. The rational for setting a_2 is shown below which shows the very high correlation between a_1 and a_2 during the Harmonisation process which essentially means that there is no independent information is parameter a_2. We have therefore set a_2 to zero.
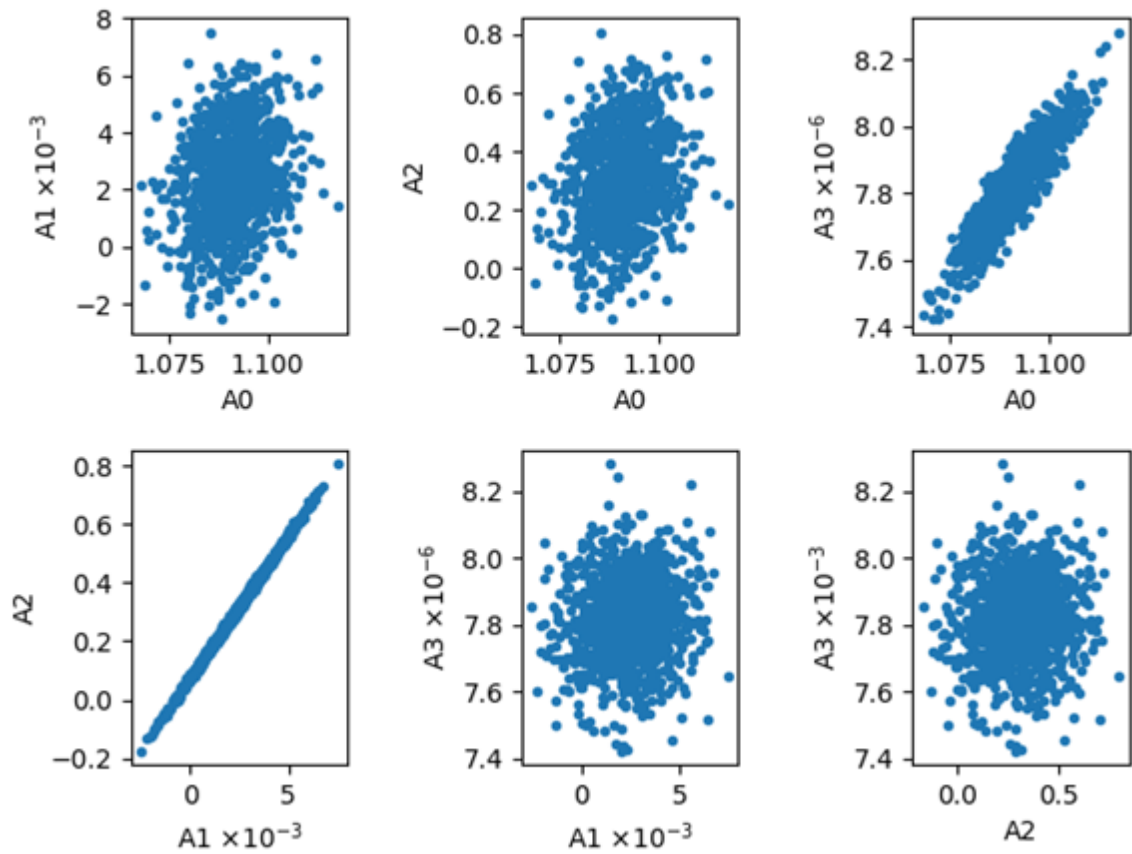
Figure 19 Correlations between harmonization parameters obtained from Monte Carlo simulation analysis. The strong positive correlation between a_2 and a_1 in the correction to the emissivity is what is behind the decision to set between $a_2=0$ in the measurement equation (Eq. 3.2).